

# Tumor-anchored deep feature random forests for out-of-distribution detection in lung cancer segmentation

Aneesh Rangnekar and Harini Veeraraghavan

*Department of Medical Physics*

*Memorial Sloan Kettering Cancer Center, 1275 York Avenue, New York City, 10065, New York, USA*

---

## Abstract

Accurate segmentation of cancerous lesions from 3D computed tomography (CT) scans is essential for automated treatment planning and response assessment. However, even state-of-the-art models combining self-supervised learning (SSL) pretrained transformers with convolutional decoders are susceptible to out-of-distribution (OOD) inputs, generating confidently incorrect tumor segmentations, posing risks for safe clinical deployment. Existing logit-based methods suffer from task-specific model biases, while architectural enhancements to explicitly detect OOD increase parameters and computational costs. Hence, we introduce a plug-and-play and lightweight post-hoc random forests-based OOD detection framework called RF-Deep that leverages deep features with limited outlier exposure. RF-Deep enhances generalization to imaging variations by repurposing the hierarchical features from the pretrained-then-finetuned backbone encoder, providing task-relevant OOD detection by extracting the features from multiple regions of interest anchored to the predicted tumor segmentations. Hence, it scales to images of varying fields-of-view. We compared RF-Deep against existing OOD detection methods using 1,916 CT scans across near-OOD (pulmonary embolism, negative COVID-19) and far-OOD (kidney cancer, healthy pancreas) datasets. RF-Deep achieved AUROC  $> 93.50$  for the challenging near-OOD datasets and near-perfect detection (AUROC  $> 99.00$ ) for the far-OOD datasets, substantially outperforming logit-based and radiomics approaches. RF-Deep maintained similar performance consistency across networks of different depths and pretraining strategies, demonstrating its effectiveness as a lightweight, architecture-agnostic approach to enhance the reliability of tumor segmentation from CT volumes.

**Keywords:** Tumor segmentation, lung cancer, computed tomography, out-of-distribution detection, random forests, outlier exposure

---

## 1. Introduction

Deep learning (DL) based medical image analysis is now applicable throughout the continuum starting from diagnosis, treatment planning, and response monitoring at follow-up to enhance care of patients with cancer. For instance, hybrid transformer-convolutional networks have shown to provide highly accurate tumor and healthy tissue segmentations from radiographic modalities (Jiang et al., 2022; Willeminck et al., 2022; Nguyen et al., 2023; Yan et al., 2023; Qayyum et al., 2023; Gu et al., 2025). DL methods for medical applications are often developed using narrowly scoped datasets. Consequently, accuracy on in-distribution (ID) testing doesn't translate to out-of-distribution (OOD) clinical cases impacted by different imaging acquisitions (Roschewitz et al., 2023; Koch et al., 2024), concept drifts (Huang et al., 2022; Sahiner et al., 2023; Gomez et al., 2025), and label shifts like varying delineation guidelines (Nichyporuk et al., 2022; Lempart et al., 2023; Godau et al., 2025). Importantly, DL models also produce confidently inaccurate predictions (Hendrycks et al., 2019; Quiñonero-Candela et al., 2022; Prabhu et al., 2022; Banerjee et al., 2023), hindering ability of clinicians to leverage model uncertainties in utilizing AI predictions for clinical decision making (Otlés et al., 2021). Over-reliance on AI models by experts carries the risk of clinical expert deskilling (Budzyń et al., 2025), exacerbating risk of harm to patients. These considerations underscore the critical need to provide reliably accurate methods that can contextualize task model predictions with respect to data instances used in prediction.

Segmentation accuracy metrics like Dice and Hausdorff distances, though useful to compare models' performance on data cohorts, do not reflect well-calibrated uncertainty estimates even on ID datasets (Ren et al., 2024; Rangnekar

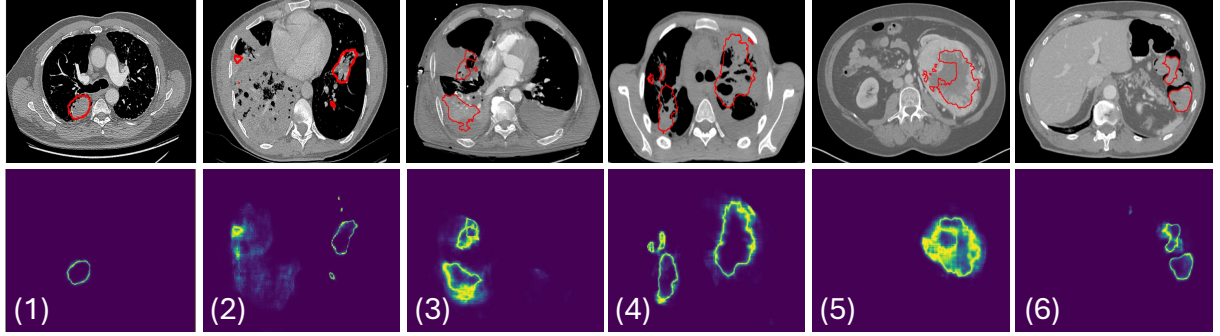


Figure 1: Uncertainty maps for in-distribution (ID) and out-of-distribution (OOD) scans. (a) ID lung cancer cases (1–2) show concentrated boundary uncertainty; OOD cases (3–6: pulmonary embolism, COVID-19-negative, kidney cancer, healthy abdomen) exhibit concentrated, diffused, or misaligned patterns.

et al., 2025). Model uncertainty visualization (Goddard et al., 2012) has been shown to enhance consistency of clinical delineations (Biase et al., 2024). However, such measures can be unreliable in OOD scenarios, as demonstrated in three out of four OOD cases in Figure 1. Methods to explicitly flag OOD scans are often narrowly scoped to detect any variation from training data (Roschewitz et al., 2023; Godau et al., 2025); the model itself cannot generalize to common image variations not encountered in training, limiting their use for practical purposes. Our work overcomes the limitations of prior approaches by leveraging pretrained models to ensure sufficient generalization to common clinical imaging variations while enhancing robustness to far-OOD (disease in different anatomical sites) and near-OOD (different disease in same anatomic site) use cases. Our contributions are:

- A post-hoc OOD detection approach using random forests with deep features (RF-Deep), trained with outlier exposure. Features are extracted from regions of interest (ROIs) anchored to the task-specific model’s predictions, enabling scan-level and task-relevant OOD filtering. Our approach reduced false detections, achieving AUROC > 90 on challenging near-OOD datasets and near-perfect detection on the far-OOD datasets.
- Generalizability to common imaging variations is ensured by using features extracted from the hierarchical encoder layers of a segmentation model subject to self-supervised learning (SSL) pretraining and task-specific fine-tuning. Robustness of task-specific model performance on commonly encountered imaging variations is also reported.
- Evaluation on 2,056 3D CT scans from five public datasets, with analysis of SSL pretraining methods, model depths, and classifier designs on OOD detection performance.
- Analysis of why RF-Deep outperforms radiomics-based and logit-based approaches by performing unsupervised clustering, SHAP-based feature importance, and spatial uncertainty analysis.

## 2. Related Works

Broadly, there are two classes of approaches for improving the generalizability of models for OOD detection. The first class consists of learner-based methods that leverage large corpus of training data, regularization techniques, and specialized network architectures to extract feature representations that are robust to data variations. The second class are filter-based methods that explicitly flag OOD cases at test time, preventing unreliable predictions and thereby improving overall reliability.

### 2.1. Learner-based methods

Learner-based methods focus on extracting robust feature representations from available training data such that the model can be applied across different domains without performance degradation. Domain-invariant feature representations can be extracted using: (a) specialized architectures (Saha et al., 2021; Simeth et al., 2023), (b) data

augmentation methods in image and feature space (Jung et al., 2019; Chen et al., 2022; Vaish et al., 2025), (c) regularized training with multi-task objectives (Panfilov et al., 2019; Wen et al., 2024), as well as (d) SSL pretraining with numerous unlabeled examples to expose models to wider ranges of imaging and data variations than is practical for supervised training (Hatamizadeh et al., 2022; Haghighi et al., 2022; Jiang et al., 2024; Du et al., 2024).

Prior works on tumor segmentation have shown that use of enhanced network architectures combining attention mechanisms and residual connections that effectively increase network size produce robust generalization across different MR acquisitions (Saha et al., 2021; Simeth et al., 2023). Another approach by Gu et al. (2021) explicitly trained a model to extract separate basis functions for various domains that were then combined using group convolutions to extract a generalizable representation applicable to unseen image domains for prostate gland segmentation.

An alternative approach to creating specialized architectures is to employ data augmentation and regularization tasks when training standard networks like the U-Net (Chen et al., 2022; Wen et al., 2024). Mixup is a type of data-agnostic augmentation strategy applicable either to the inputs, labels, as well as feature representations extracted from the input images (Jung et al., 2019; Vaish et al., 2025). Advanced feature augmentation strategies using normalizing flows extract feature statistics for creating augmented features in individual layers, enhancing domain generalization for prostate gland and eye fundus segmentation (Safdari et al., 2025). Conceptually, the mixup and augmentation methods are general and could be combined with transformers to further enhance robustness to distribution shifts (Boone et al., 2023).

SSL pretraining is an altogether different approach compared to prior methods that employs multi-stage training to fully exploit the image information to extract distribution shift robust feature representations. This is accomplished either through pretraining with extensive data augmentations (Fedorov et al., 2021) or simply by exposing the model to a large corpus of unlabeled examples encompassing possible imaging variations (Hatamizadeh et al., 2022; Jiang et al., 2024; Gomez et al., 2025). A different approach is a successive training strategy that explicitly addresses generalization to OOD by converting a portion of every encountered OOD data to ID data and successively refines the model to that dataset (Azizi et al., 2023). Unlike SSL, which aims to reduce need for large downstream datasets, this requires data for adapting to every new domain.

## 2.2. Filter-based OOD methods

Whereas learner-based methods seek to enhance models’ consistency across domains subject to distribution shifts, filter-based methods aim to enhance the confidence of predictions by filtering out data that differs from the training distribution. For this purpose, filter-based methods implement either a separate OOD model or a task-integrated OOD model to identify OOD data scans. Scans detected as OOD are removed, ensuring that models are applied only on ID-like data where predictions and uncertainties are valid, providing reliably safe performance required in clinical settings (Berger et al., 2021).

Similar to learner-based methods, filter-based methods have been applied to handle imaging acquisition differences (Tardy et al., 2019; Gao and Wu, 2020; Nandy et al., 2021). The vast majority of filter-based methods focused on disease classification from 2D images; method complexity varied from easy-to-compute Mahalanobis distances (Tardy et al., 2019), dedicated networks for detecting OOD cases (Nandy et al., 2021) to more complex instance-level re-training performed to assign metric distance to OOD scans by measuring response variations on the ID test set (Gao and Wu, 2020). A different approach involves using a single model to classify tasks on inlier data, while exposing the same model to outlier examples to detect OOD during inference (Araujo et al., 2023; Roy et al., 2022). The last approach is practical to implement when OOD cases are known as domain knowledge (e.g. optical tomography versus retinal fundus images) (Araujo et al., 2023), or when the outliers like infrequent disease conditions are deducible from the training as OOD (Roy et al., 2022).

Similar to classification tasks, Mahalanobis distance computed from feature embeddings has been used to detect OOD for lung lesion segmentation on CT scans of patients with COVID-19 (González et al., 2022). However, the high dimensionality of feature embeddings limits accuracy (Roy et al., 2022), due to difficulty in distinguishing subtle differences in appearance of different pathologies occurring in the same disease site (Berger et al., 2021). Dimensionality reduction methods including PCA (Woodland et al., 2024) as well as VQ-GAN (Graham et al., 2023; Pinaya et al., 2022) have been used to reduce the latent space and sharpen the separation of ID from OOD feature distributions. However, dimensionality reduction can suffer from high inductive bias (Nalisnick et al., 2019), reducing applicability to wider range of OOD scans. These dimensionality reduction approaches, including GANs, also require

additional training with secondary datasets. Calibrated uncertainty estimation methods using computationally simple temperature scaling (Karimi and Gholipour, 2022) as well as logit-based OOD scores (Hendrycks and Gimpel, 2017; Hendrycks et al., 2022) have been used for OOD detection. However, effectiveness of such methods are limited by inherent bias of the task-specific model use to estimate uncertainty (Mehrtash et al., 2020). Modified architectural formulations (Yuan et al., 2023; Larrazabal et al., 2023) and generative diffusion methods (Nguyen et al., 2026) to detect OOD increase network parameters and require additional training. Finally, radiomic feature distance methods though useful for OOD detection at cohort level (Konz et al., 2024; Vasiliuk et al., 2023) are not applicable to scan-level detections due to their difficulty in extracting subtle data variations while providing robust performance over common variations.

### 3. Framework overview and OOD task definition

Our goal for OOD detection was to develop a highly accurate scan-level OOD detection approach, which does not require large numbers of outlier samples, with generalizable applicability to images with different acquisitions and fields of view. Let  $\mathcal{D}_{\text{in}}$  denote the distribution of lung cancer CT scans, closely matching the training dataset used to create the lung tumor segmentation model, and let  $\mathcal{D}_{\text{out}}$  represent the scans that differ in pathology and anatomic sites. The objective is to determine whether a new scan  $x$  belongs to  $\mathcal{D}_{\text{in}}$  or  $\mathcal{D}_{\text{out}}$  at the scan level via a scoring mechanism provided by the random forest classifier.

Our approach combines the advantages of learner-based methods (by using the backbone of a segmentation model subject to SSL pretraining to extract imaging domain-agnostic features) with a filter-based classifier to reject conceptually different scans. An architecturally simple and lightweight random forest OOD classifier incorporates known outliers during training (Hendrycks et al., 2019; Thulasidasan et al., 2021; Guha Roy et al., 2022) to enhance the classifier’s ability to flag unseen outliers. Scan-level OOD prediction for segmentation involves thousands of voxel-level predictions, which, while offering rich spatial context, also introduces memory constraints in processing and aggregating information from their large 3D volumes. Our approach addresses this issue by focusing the OOD detection in regions of interest (ROI) anchored to the predicted tumor segmentation, and then averaging the metric scores from those regions, which also allowed the approach to scale to images with varying field of views. Using regions anchored near the predicted tumors also allows the model to focus on differentiating features in relevant parts of the image, as opposed to distinguishing entire images, which in turn allows it to distinguish pathologies occurring in the same disease site.

#### 3.1. Segmentation model

The segmentation framework employs a hybrid transformer-convolution architecture to leverage strengths of global contextual modeling with the transformer backbone as encoder and local spatial precision of the convolutional decoder. The backbone is a hierarchical Swin Transformer (Liu et al., 2021) with depth configuration 2 – 2 – 12 – 2 across four successive stages, with a patch size of  $2 \times 2 \times 2$  voxels and a window size of  $4 \times 4 \times 4$  voxels. Its hierarchical design progressively aggregates features at multiple spatial scales to capture fine-grained anatomical details. Windowed self-attention within each stage reduces complexity while preserving details and global context, critical for processing large volumetric images of size  $128 \times 128 \times 128$  voxels. The backbone was pretrained with the self-distilled masked image transformer (SMIT) framework to enhance robustness to imaging and patient variations (Jiang et al., 2022). SMIT combines masked image prediction (He et al., 2021; Xie et al., 2022) with self-distillation (Zhou et al., 2022); described in Appendix Appendix A. The decoder, a 3D U-Net-based (Ronneberger et al., 2015) convolutional structure, was randomly initialized and fine-tuned with ID task-specific dataset. Following training, the entire model is frozen (🔒) for subsequent segmentation and features-based OOD detection.

#### 3.2. Scan-level OOD detection approach

Our OOD detection pipeline consists of the following four steps (Figure 2):

- **Regions of interest extraction:** The task-specific segmentation model (Subsection 3.1) was used to generate segmentation of tumors from the entire scan. Detected tumor regions from each scan were used to extract multiple 3D ROIs, ensuring the tumor appears within each ROI volume without precise centering (Figure 2a).

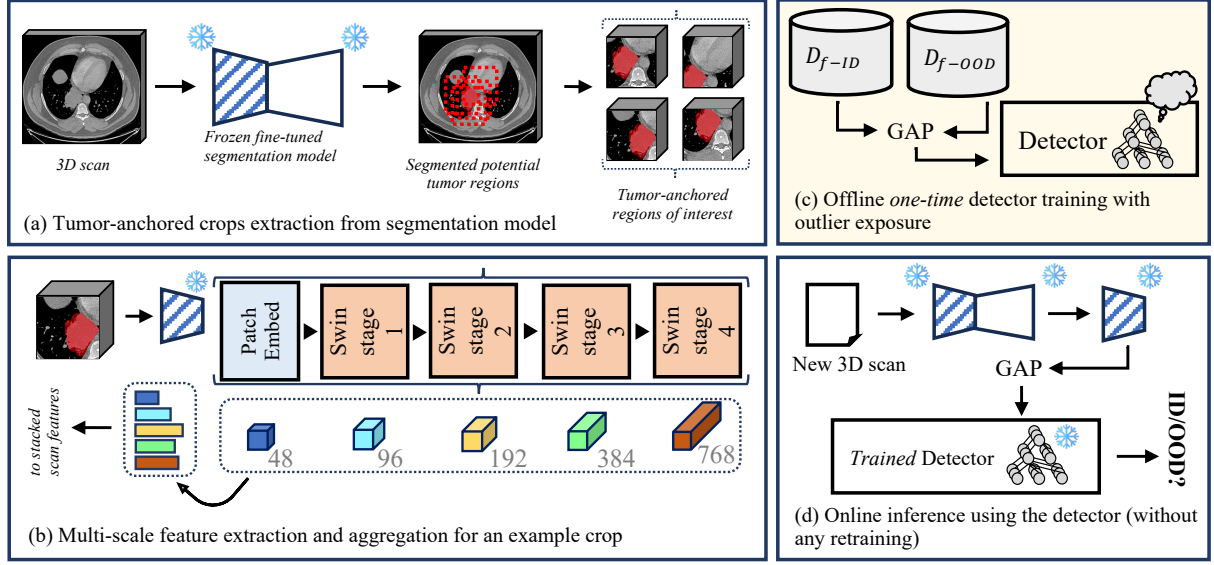



Figure 2: RF-Deep workflow for scan-level OOD detection. Panels (a–c) depict feature extraction from the frozen  segmentation model and random forest training in an outlier exposure manner and panel (d) shows scan-level ID/OOD inference using the trained detector.

- **Feature extraction.** We repurposed the fine-tuned backbone encoder from the segmentation model to extract multi-scale features from the five encoder stages: the patch embedding layer (48 channels) and the four Swin Transformer stages (96, 192, 384, and 768 channels, respectively). All features were aggregated into a single scan-level descriptor through global average pooling (GAP) describing the scan as a vector of features (Figure 2b).
- **Training the OOD detector.** Feature vectors were extracted from ID lung cancer datasets as well as a representative set of OOD scans from tumor anchored regions as described above and used to train the RF classifier for each cohort once. This approach enabled our detector to learn subtle decision boundaries that distinguish shifts even between different diseases affecting the same anatomic region (Figure 2c).
- **Online inference.** Given a new test instance, the aforementioned pipeline extracts potential tumor regions and tumor-anchored ROIs, followed by the extraction of GAP features, which the RF classifier uses to generate scan-level OOD classification (Figure 2d).

## 4. Experiments setup

### 4.1. Implementation details

All models were implemented in PyTorch (Paszke et al., 2019) and MONAI (Cardoso et al., 2022). All scans were intensity-normalized using the lung window (Hounsfield units (HU):  $[-400, 400]$ ) and resampled to a uniform voxel spacing of  $1 \text{ mm}^3$ .

**Segmentation.** Models were fine-tuned using cross-entropy and Dice loss with a batch size of 16 distributed across four NVIDIA GPUs, with an input size of  $128 \times 128 \times 128$  voxels. We used a learning rate of  $2 \times 10^{-4}$  with linear warm-up (50 epochs) and cosine annealing over 1,000 epochs. Data augmentations included random flips, rotations, affine transformations, and illumination adjustments, consistent with Tang et al. (2022); Jiang et al. (2022). For inference on the full scan volume, we used a sliding window with 50% Gaussian overlap to obtain the segmentations.

**OOD Detection.** Random forest classifiers employed 1,000 trees with a maximum depth of 20 and balanced class weights (using default scikit-learn hyperparameters). We extracted deep feature representations from  $n = 4$  tumor-anchored 3D ROIs per scan for all ID and OOD datasets. All ROIs were used individually during training to increase training samples, and probabilities from all ROIs were averaged at the scan level as an ensemble for inference. For

MaxSoftmax, MaxLogit, and energy, scan-level scores were obtained by mean-aggregating tumor (positive class) predictions across all voxels using the corresponding metric.

#### 4.2. Datasets

**Backbone pretraining.** The backbone encoder was pretrained using the self-distilled masked image transformer (SMIT) framework on 10,432 3D CT scans, encompassing public and institutional datasets, following Jiang et al. (2022); Tang et al. (2022); Jiang et al. (2024).

**Comparison to other pretraining strategies and architectures.** Additionally, we pretrained using SimMIM (Xie et al., 2022), iBOT (Zhou et al., 2022), and Swin UNETR (Tang et al., 2022) to assess the impact of pretraining strategy on both accuracy and OOD robustness. To analyze the effect of model depth, we pretrained a lite backbone configuration (2 – 2 – 2 – 2) using SMIT. Finally, we evaluated the publicly available Swin UNETR pretrained checkpoint (marked as <sup>†</sup>) to assess the impact of pretraining data.

**Fine-tuning.** We combined the pretrained backbone as the encoder with a randomly initialized U-Net decoder and fine-tuned using  $N = 317$  3D scans from publicly available non-small cell lung cancer (NSCLC) Radiomics dataset (Aerts et al., 2015) with radiologist-provided tumor delineations.

**Testing.** We used the NSCLC Radiogenomics dataset (Bakr et al., 2017), consisting of 140 images from various scanners (GE, Siemens), as the ID test set. OOD evaluation used 1,916 3D CT scans from four public datasets: pulmonary embolism (RSNA PE,  $N = 1,225$ ) (Colak et al., 2021), COVID-19 negative patients (MIDRC C19,  $N = 120$ ) (Tsai et al., 2021), kidney cancer (KiTS,  $N = 489$ ) (Heller et al., 2023), and healthy scans of the pancreas (PancreasCT,  $N = 82$ ) (Roth et al., 2015). The near-OOD datasets (RSNA PE, MIDRC C19) consist of chest CTs involving non-cancerous pathologies such as pulmonary embolism and inflammation, depicting appearances similar to lung lesions. The far-OOD datasets (KiTS, PancreasCT) include cases with larger field-of-view than training with healthy organs and non-lung cancers.

#### 4.3. Evaluation metrics

Segmentation accuracy on ID datasets was measured using the Dice similarity coefficient (DSC) and the 95th percentile Hausdorff distance (HD95). OOD detection accuracy was computed using the area under the receiver operating characteristic curve (AUROC) and false positive rate at 95% true positive rate (FPR at 95% TPR, or FPR95). AUROC quantifies the separability between ID and OOD cases (Davis and Goadrich, 2006), with higher values indicating better discrimination and FPR95 measures the proportion of OOD cases misclassified as ID when sensitivity is fixed at 95% (Liang et al., 2018), where lower values are better.

To ensure meaningful AUROC computation, the number of OOD scans was balanced with ID test cases ( $N = 140$ ) by sampling OOD examples with replacement in datasets (RSNA PE and KiTS) with a much larger number of OOD scans and averaging the computed metrics across multiple draws. Splits ensured zero patient overlap with consistent OOD case counts across runs. This evaluation approach avoids biases from imbalanced evaluation sets while ensuring stable ID-OOD ratios, following best practices for robust OOD evaluation (Szyc et al., 2023; Humblot-Renaux et al., 2023).

For segmentation performance, we reported the mean and standard deviation across test cases. For OOD detection performance, we reported the point estimates with 95% bootstrap confidence intervals computed over 100 runs with matched random seeds to reflect sampling variability across different train-validation splits.

#### 4.4. Comparative OOD detection methods

Baseline comparisons included commonly used OOD detection methods, namely, MaxSoftmax (Hendrycks and Gimpel, 2017), MaxLogit (Hendrycks et al., 2022), and energy (Liu et al., 2020), performed by computing scan-level scores by mean-aggregating the tumor (positive class) predictions across all voxels (see Appendix Appendix B).

In addition, a RF classifier was created using handcrafted radiomics features ( $N = 293$ ) called RF-Radiomics, computed within the segmented tumor regions following the Image Biomarker Standardization Initiative (IBSI) guidelines (Zwanenburg et al., 2020) with open-source software PyCERR (Apte et al., 2018). Details of individual radiomic features are in Table C.5. The high correlation among radiomic features was addressed by employing recursive feature elimination to select a more compact and informative set of radiomic features. Of note, recursive feature elimination was not used for training the RF-Deep classifier.

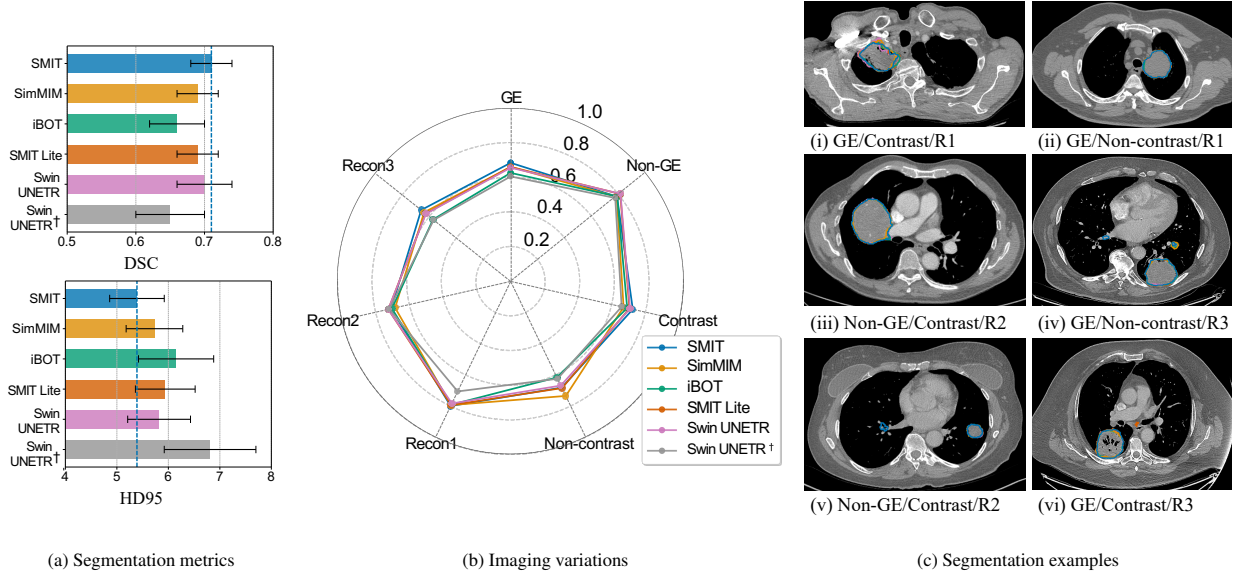


Figure 3: Pretraining strategies performance and robustness evaluation on ID test set. (a) Segmentation metrics (DSC and HD95). (b) Performance across imaging variations. (c) Representative segmentations;  $R$  denotes reconstruction kernel.

Finally, the Mahalanobis distance-based OOD detector (MD-Deep) (Lee et al., 2018) was computed with respect to deep features of the ID data, modeled as a single Gaussian in feature space using Ledoit-Wolf covariance estimation. Hence, MD-Deep computes OOD scores as the distance of the each scan with respect to the fitted ID distribution. We excluded ODIN (Liang et al., 2018), as it requires temperature scaling and gradient perturbations on fine-tuning data, which in real clinical settings is often unavailable when applied to new OOD cohorts.

## 5. Results

### 5.1. Segmentation performance on ID datasets

Segmentation performance for the various analyzed pretraining strategies is shown in Figure 3a for the ID testing dataset. All pretrained methods were similarly accurate, with the lowest accuracies produced by iBOT, followed by the publicly available Swin UNETR† checkpoint.

Next, we performed a disaggregated analysis of model performance under common imaging variations including scanner manufacturer (GE versus non-GE), contrast versus non-contrast enhanced CT, and reconstruction kernels. Reconstruction kernels were categorized as Recon 1 (GE ‘standard’ and ‘bone’, Siemens with  $< B40$ ), Recon 2 (GE ‘Bone Plus’, Siemens with  $\geq B40$  and  $< B50$ ), and Recon 3 (GE ‘Lung’, Siemens  $\geq B50$ ). Model fine-tuning was performed on the public dataset acquired on Siemens scanners with contrast and Recon 1 kernel. From Figure 3b, all models were similarly accurate across the analyzed variations, with larger gaps in accuracy noted for Swin UNETR† (Recon 1, non-contrast CT) and iBOT (Recon 3, non-contrast). All other strategies showed relatively small degradation in accuracy due to the analyzed variations indicating robust performance through any of the pretrained methods. SMIT and SMIT Lite strategies were similarly accurate, indicating that a smaller model is sufficient for robust tumor segmentation. On the other hand, choice of pretraining data impacted accuracy, as seen by the performance difference between the Swin UNETR trained with the 10K dataset and the public checkpoint Swin UNETR. Detailed accuracies using DSC and HD95 metrics for the analyzed methods are shown in Figure C.10.

Overall, the SMIT-pretrained model was the most accurate, followed by the Swin UNETR method, and was thus selected for benchmarking the OOD detection method using RF-Deep throughout this paper.

Table 1: OOD detection performance comparing various methods on the segmentation model fine-tuned using the SMIT-pretrained backbone. AUROC ( $\uparrow$ ) and FPR95 ( $\downarrow$ ) are reported with 95% bootstrap confidence intervals over 100 matched-seed runs.

Method	RSNA PE		MIDRC C19		KiTS		PancreasCT	
	AUROC	FPR95 %	AUROC	FPR95 %	AUROC	FPR95 %	AUROC	FPR95 %
MaxSoftmax	88.61	38.37	86.57	49.27	95.67	23.26	94.61	34.27
	(84.62–92.36)	(31.78–49.24)	(81.79–90.14)	(39.53–59.78)	(93.41–98.06)	(11.47–34.19)	(92.61–97.49)	(24.80–49.30)
MaxLogit	88.77	40.01	89.31	41.59	95.89	18.05	93.53	30.87
	(85.09–92.43)	(24.80–52.52)	(85.05–93.06)	(29.84–53.96)	(93.58–98.44)	(10.41–27.37)	(90.17–96.59)	(16.17–56.87)
Energy	88.59	39.86	89.30	43.04	95.80	17.47	93.52	29.96
	(84.85–92.24)	(24.80–52.55)	(84.98–93.04)	(29.84–55.43)	(93.41–98.44)	(10.41–26.65)	(90.10–96.53)	(15.83–56.87)
RF-Radiomics	88.70	41.10	91.30	30.00	96.20	11.80	96.10	17.20
	(81.50–93.00)	(25.20–57.80)	(87.10–94.40)	(17.40–45.60)	(93.00–98.30)	(5.80–21.90)	(89.10–99.20)	(4.30–41.90)
MD-Deep	87.30	45.10	84.50	58.50	99.20	3.10	99.20	2.80
	(83.90–91.10)	(30.60–60.30)	(79.40–89.00)	(38.20–77.60)	(97.90–99.80)	(0.00–9.20)	(98.20–100.00)	(0.00–7.70)
<b>RF-Deep</b>	<b>95.80</b>	<b>15.20</b>	<b>93.30</b>	<b>25.50</b>	<b>100.00</b>	<b>0.10</b>	<b>100.00</b>	<b>0.00</b>
	(92.60–98.50)	(7.10–23.50)	(89.90–96.00)	(16.80–36.20)	(99.90–100.00)	(0.00–1.00)	(100.00–100.00)	(0.00–0.00)

## 5.2. Out-of-distribution detection performance

RF-Deep is the most accurate method for both near-OOD and far-OOD datasets (Table 1). On the near-OOD datasets (RSNA PE and MIDRC C19), RF-Deep achieved AUROCs of 95.80 and 93.30, outperforming the next best method (MaxLogit) by approximately 7.7% and 4.0%, respectively. Similarly, RF-Deep reduced FPR95 by 18–25 absolute points compared to the next closest competitor. These improvements remain consistent within the 95% confidence intervals, with non-overlapping intervals confirming statistically significant superiority over all baseline methods, highlighting the stability of RF-Deep across bootstrap resampling.

RF-Deep also achieved near-perfect separability on the far-OOD datasets using KiTS (AUROC 100, FPR95 0.10%) for kidney cancers and PancreasCT (AUROC 100, FPR95 0.00%) containing healthy abdominal scans, effectively eliminating false alarms for anatomically distant pathologies. Although it was less accurate on the near-OOD cohorts compared to its accuracy on the far-OOD cohorts, the gap in AUROC (RSNA PE: +3.5%, MIDRC C19: +6.7%) was the smallest compared to all other methods, with the next smallest gap observed for RF-Radiomics (RSNA PE: +7.5%, MIDRC C19: +4.9%).

RF-Radiomics, while competitive on the far-OOD datasets (AUROC of 96.20 on KiTS and 96.10 on PancreasCT with relatively low FPR95), produced moderate error rates on the near-OOD cohorts (AUROCs 88.70 and 91.30, FPR95s around 30–41%), indicating that handcrafted features are less effective than deep features at capturing subtle differences in the appearance of pathologies (analyzed further in Sections 5.3.1 and 5.3.2).

MD-Deep, although highly accurate for detection on far-OOD datasets (AUROC 99.2 on both KiTS and PancreasCT) was less effective and similar to logit-based methods on near-OOD cohorts (AUROC 87.3 on RSNA PE and 84.5 on MIDRC C19, with FPR95 around 45–59%). MD-Deep was also less accurate than RF-Deep on near-OOD datasets, despite both methods using identical encoder features, indicating that feature selection performed by the RF was essential to achieve better separation of ID from OOD scans. Additional evaluation to assess if feature reduction enhanced performance showed no improvement compared to the standard MD-Deep approach (Figure C.11).

All logit-based methods showed a considerable drop in accuracy for the near-OOD datasets compared to their performance on far-OOD datasets, reflecting the challenge in detecting OOD from images depicting different pathologies but from the same disease site as the ID dataset. For instance, MaxLogit exhibited performance gaps of 7–8% between near-OOD and far-OOD datasets, more than twice the gap observed for RF-Deep (3.5–6.7%), suggesting that logit-based scores alone may be insufficient for challenging near-OOD detection. We analyzed the underlying causes of these performance differences in Section 5.3.3.

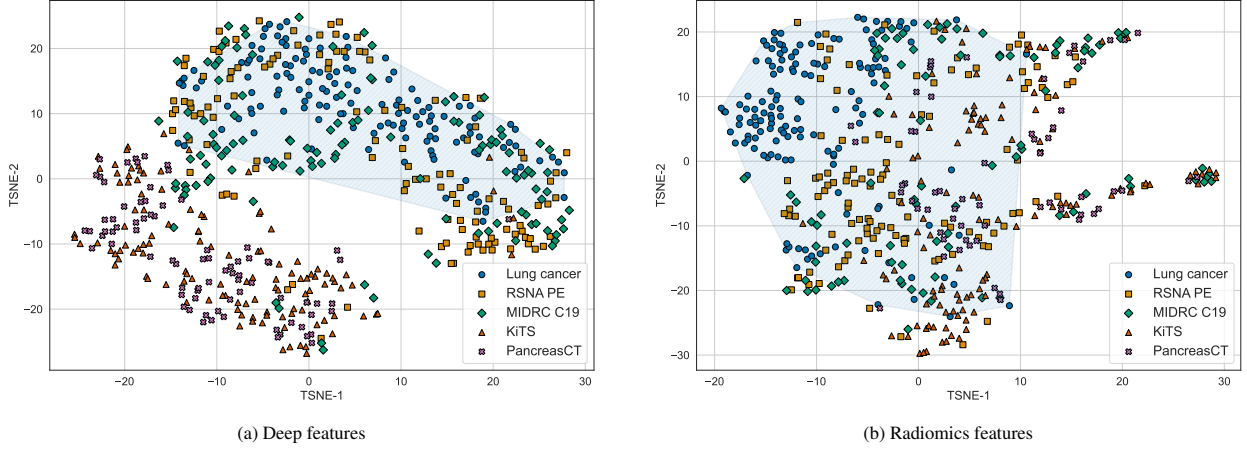


Figure 4: t-SNE projected embeddings showing dataset-wise separability of (a) deep features and (b) radiomics features. Results from one representative split (of 100), combining all datasets in a single visualization, are shown for brevity. The shaded blue regions indicate the convex hull of the ID dataset.

### 5.2.1. Impact of model pretraining on OOD detection

Next, we analyzed whether the choice of model pretraining, model size (SMIT versus SMIT Lite), and pretraining data (Swin UNETR versus Swin UNETR<sup>†</sup>) impacted the accuracy of RF-Deep. RF-Deep remained the most accurate method across all backbone architectures (Table C.6), consistently achieving near-perfect accuracy on the far-OOD datasets. Table C.7 further demonstrated that RF-Deep’s superiority over logit-based and radiomics methods was consistent across all tested backbones, with RF-Deep outperforming the next best method by large margins on the near-OOD datasets. Accuracy differences between the SMIT and SMIT Lite models on the near-OOD cohorts were modest (RSNA PE AUROC: 93.7 vs 94.1; MIDRC C19 AUROC: 93.2 vs 90.4; RSNA PE FPR95: 17.6% vs 20.4%; MIDRC C19 FPR95: 26.5% vs 30.5%), with SMIT Lite showing slightly better performance on RSNA PE but marginally lower accuracy on MIDRC C19.

Similarly, RF-Deep performance for Swin UNETR and Swin UNETR<sup>†</sup> backbones was comparable (RSNA PE AUROC: 90.4 vs 89.6; MIDRC C19 AUROC: 88.6 vs 88.9; RSNA PE FPR95: 41.5% vs 34.1%; MIDRC C19 FPR95: 35.8% vs 37.5%). However, both Swin UNETR methods exhibited 4–7% lower AUROC on the near-OOD datasets compared to SMIT-based models, reaffirming that pretraining strategy and encoder architecture substantially influence OOD detection performance within the RF-Deep framework.

## 5.3. Why RF-Deep outperforms alternatives

### 5.3.1. RF-Deep extracts features that are better separated than RF-Radiomics

Figure 4 visualizes the t-SNE embeddings (perplexity=30, 1,000 iterations) of deep features (panel a) and radiomics features (panel b) for the ID and OOD datasets collectively. RF-Deep features exhibit better cluster separation between the ID and OOD datasets, with minimal overlap between ID and anatomically distinct far-OOD datasets (KiTS, PancreasCT) and moderate overlap with near-OOD datasets (RSNA PE, MIDRC C19), consistent with their increased detection difficulty. Radiomics features produced poorly separated clusters for the various datasets particularly for the near-OOD datasets with respect to the ID cases, explaining the relatively lower accuracies (Table 1), and less compact OOD score distributions than RF-Deep between ID and OOD datasets as shown in Figure 5.

We next evaluated whether deep features produced by other pretraining strategies achieved similar separability as the SMIT-pretrained model. As shown in Figure C.12, all pretraining methods improved separability compared to handcrafted radiomics features. However, class separation was slightly better using SMIT-based RF-Deep compared to SMIT Lite-based RF-Deep. The differences in class separation were more pronounced between Swin UNETR and Swin UNETR<sup>†</sup>, than among SMIT, SimMIM, and iBOT, indicating the larger impact of pretraining data rather than the pretraining approach itself.

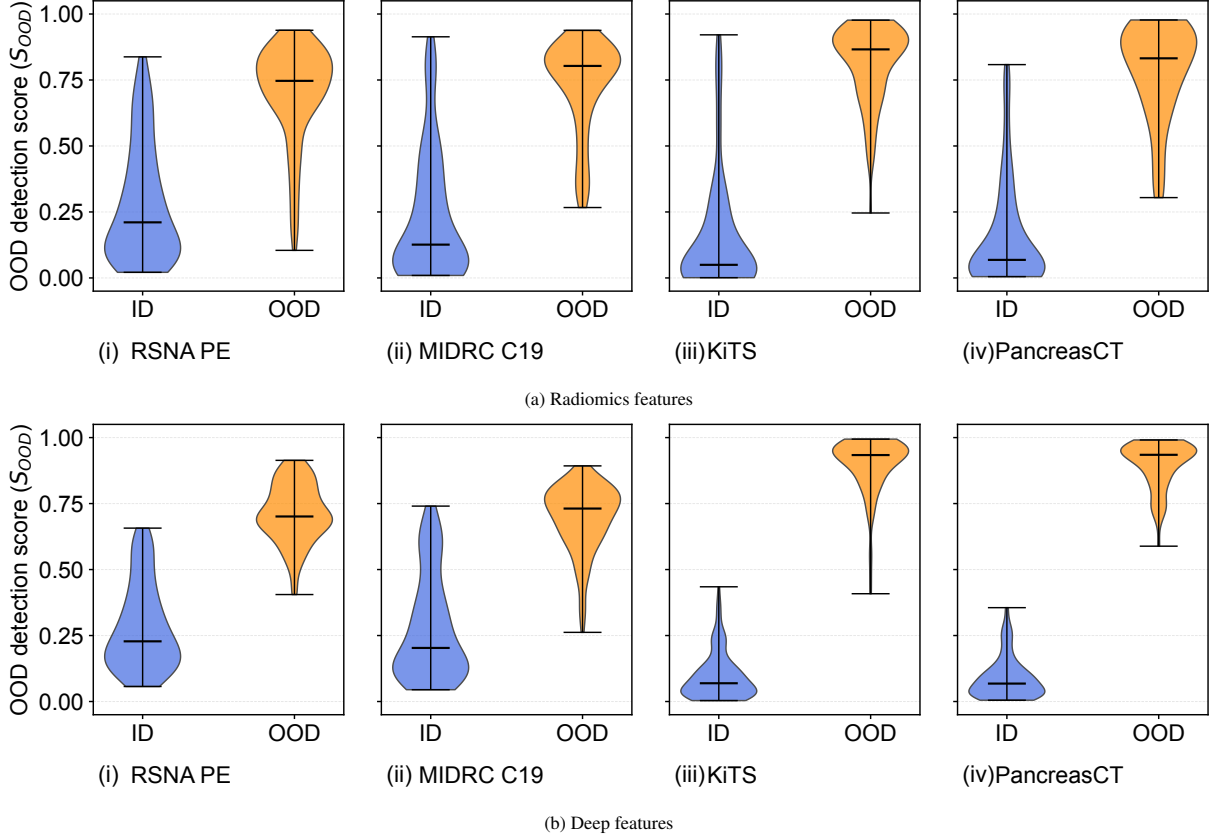


Figure 5: Scan-level OOD detection score distributions for RF-Radiomics (a) and RF-Deep (b) across 100 matched-seed runs.

### 5.3.2. RF-Deep extracts OOD data-agnostic and specific features for improved separability

We used SHAP (SHapley Additive exPlanations) (Lundberg and Lee, 2017) to identify which features drive RF-Deep and RF-Radiomics predictions, revealing how the two approaches differ in their decision-making mechanisms. Deep features (Figure 6) show broad, dataset-specific spread of important dimensions, with some features reused across multiple datasets (Ft 65, Ft 131, Ft 179, Ft 319), suggesting they capture general distributional properties relevant to distinguishing ID from OOD scans. Other features activate selectively for specific distribution shifts (e.g., Ft 5 and Ft 1381 for far-OOD), indicating that RF-Deep adapts its decision boundaries to the characteristics of each OOD scenario rather than relying on a fixed, universal subset of features. Notably, only a small fraction of the 1,488 encoder features appear consistently useful across OOD datasets, underscoring the need for outlier data exposure, especially in near-OOD scenarios where subtle feature combinations are required to distinguish concept shifts.

By contrast, radiomics features (Figure 7) emphasized shape-based and texture-based descriptors, specifically the Gray-Level Co-occurrence Matrix (GLCM) and Gray-Level Run-Length Matrix (GLRLM) subsets. While radiomic features lend interpretability compared to deep features, they are insufficient to capture the subtle differences across the datasets to accurately detect OOD.

### 5.3.3. Why logit-based spatial uncertainties are less accurate than RF-Deep?

To understand why logit-based OOD detectors were less accurate than RF-Deep, we analyzed MaxLogit spatial patterns within predicted tumor regions. We extracted boundary regions as a ring of 3 voxel thickness by performing erosion followed by dilation, each using a radius of 1 voxel. The interior contour following the erosion operation constituted the interior regions.

MaxLogit scores of ID and OOD scans show strong overall separation (Mann-Whitney U tests, all  $p < 0.001$ , effect sizes ranging from  $r = -0.75$  for MIDRC C19 to  $r = -0.90$  for KiTS) due to higher overall MaxLogit scores for

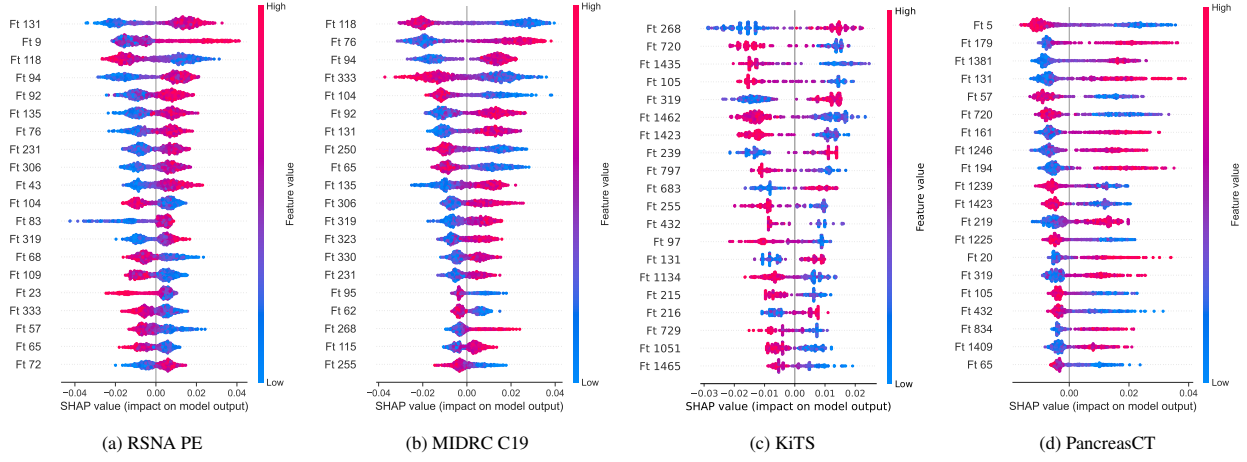


Figure 6: SHAP feature importance for RF-Deep across OOD datasets using the SMIT-pretrained segmentation model. Different deep features are activated for different distribution shifts.

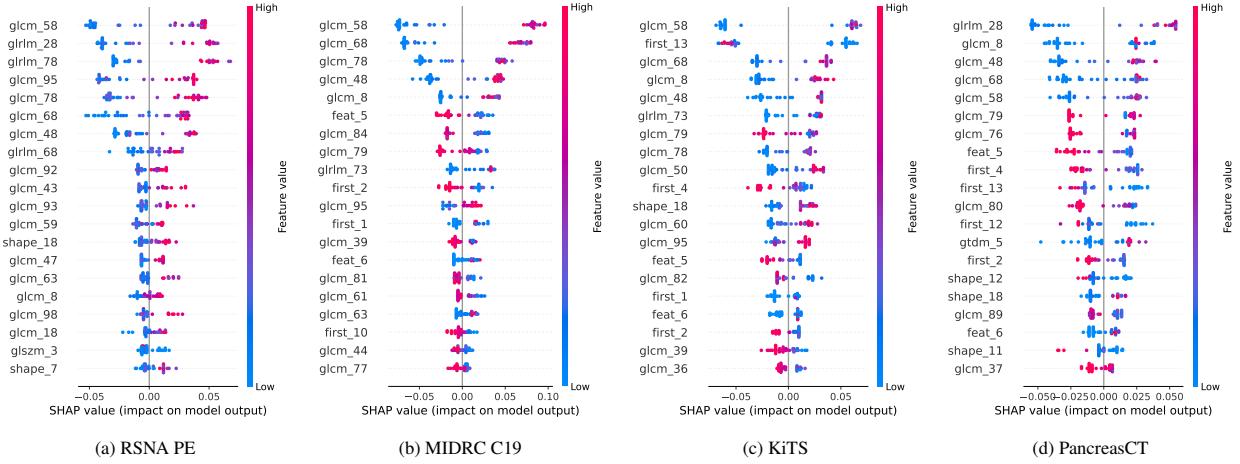


Figure 7: SHAP feature importance for RF-Radiomics across OOD datasets using segmentations from the SMIT-pretrained model. RF-Radiomics primarily relies on GLCM and GLRLM texture descriptors.

ID cases than individual OOD datasets (Table 2). However, the scores have substantially overlapping ranges with ID (ID: 0.12–4.33, RSNA PE: 0.09–3.67, MIDRC C19: 0.30–2.70).

Concretely, interior voxels showed consistently higher MaxLogit scores than the boundary voxels in both ID and OOD predictions. For ID scans, the interior scores were roughly three times higher than boundary scores, and this ratio persists across all OOD datasets despite their lower absolute scores. Paired, two-sided Wilcoxon signed-rank tests comparing interior and boundary scores within each dataset confirmed the universality of this spatial pattern ( $p < 0.001$  for all datasets, effect sizes  $r \approx -1.0$ ), indicating that the boundary–interior relationship is preserved regardless of ID or OOD status, further limiting their discriminative power.

Figure 8 provides a visualization of the MaxLogit spatial uncertainties for four representative cases. The density-normalized histograms depict the distribution of MaxLogit values in the interior and boundary regions of the detected lesions. The interior and boundary regions show very good separation for the ID case (row 1) and sufficiently different spatial distribution for the second case (row 2), enabling correct detection of OOD for this case. However, the third case (row 3) presents a challenge wherein the spatial uncertainty distribution closely resembles that of the ID case, resulting in incorrect classification. In contrast, RF-Deep correctly identified both OOD scans, demonstrating its superior ability to capture contextual features beyond local spatial patterns. Of note, both RF-Deep and MaxLogit-

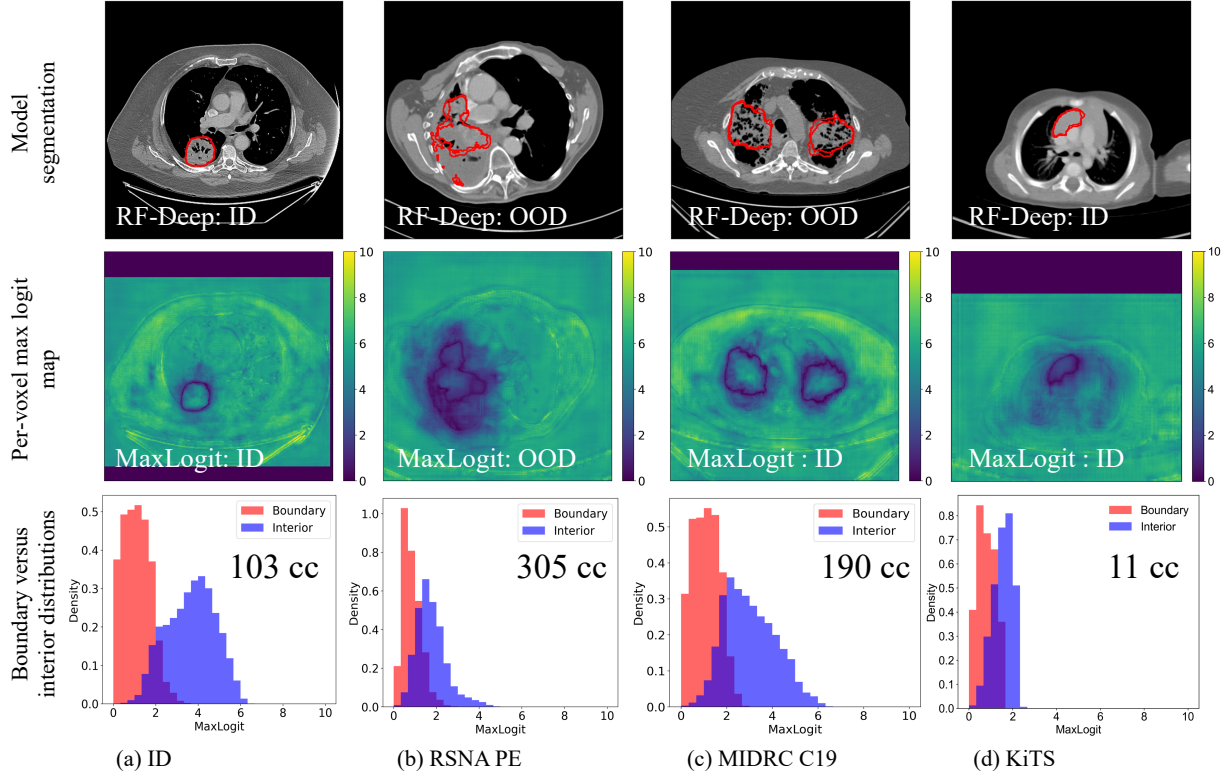


Figure 8: Representative MaxLogit visualizations for (a) segmentation predictions, (b) spatial heatmaps, and (c) boundary vs. interior distributions with predicted tumor volumes. Violet regions indicate unevaluated voxels due to foreground thresholding.

based OOD prediction was wrong for the fourth case (row 4), presenting a limiting case for either method.

An additional limitation of logit-based methods is their inherent scale invariance: MaxLogit scores reflect local appearance characteristics independent of lesion size as shown by the distributions for lesions of varying sizes in Figure 8. This is because MaxLogit computation treats voxels identically based on softmax probabilities, ignoring volumetric context that could differentiate true tumors from anatomically implausible detections. This scale invariance poses a critical bottleneck for OOD detection, as many false-positive detections on OOD scans manifest as small, scattered regions with locally high confidence but globally inconsistent spatial distributions. A method like RF-Deep on the other hand, aggregates features from regions encompassing detections, reducing the impact of tumor size variations.

#### 5.4. Framework generalization

##### 5.4.1. Effect of classifier selection

Table 3 compares different classifiers applied to the same set of encoder features. While linear probing and multilayer perceptron (MLP) classifiers, both implemented with default settings from scikit-learn, provide reasonable separability on the far-OOD cohorts, their performance degrades notably on the near-OOD cohorts (AUROC  $\approx 92 - 93\%$ , FPR95  $\approx 28 - 30\%$ ). In contrast, random forests achieve the best performance across all cohorts, highlighting the advantage of tree-based non-linear classifiers for capturing complex decision boundaries, particularly when distribution shifts are subtle (Figure 4a). The perfect performance on KiTS and PancreasCT (AUROC = 100%, FPR95  $\approx 0\%$ ) reflects the very easy nature of far-OOD detection when anatomical regions differ substantially from the training distribution.

Table 2: MaxLogit scores across ID and OOD datasets within predicted tumor (positive class) regions, stratified into overall, boundary, and interior voxels.

Dataset	Overall	Boundary	Interior
ID	2.63 $\pm$ 0.80	1.13 $\pm$ 0.35	3.25 $\pm$ 0.92
RSNA PE	1.42 $\pm$ 0.56	0.74 $\pm$ 0.25	1.92 $\pm$ 0.62
MIDRC C19	1.27 $\pm$ 0.70	0.82 $\pm$ 0.41	2.01 $\pm$ 0.73
KiTS	1.09 $\pm$ 0.40	0.85 $\pm$ 0.34	1.57 $\pm$ 0.49
PancreasCT	1.08 $\pm$ 0.60	0.66 $\pm$ 0.32	1.55 $\pm$ 0.75

Table 3: Classifier comparison on the pooled deep features. Point estimates of AUROC ( $\uparrow$ ) and FPR95 ( $\downarrow$ ) are reported over 100 matched-seed runs.

Dataset	Linear Probing	MLP Classifier	Random forest
RSNA PE	92.76 / 28.00	93.01 / 19.31	<b>95.80 / 15.20</b>
MIDRC C19	92.36 / 29.46	92.88 / 27.88	<b>93.30 / 25.50</b>
KiTS	98.92 / 0.110	99.47 / 2.490	<b>100.0 / 0.10</b>
PancreasCT	99.94 / 0.460	99.25 / 0.800	<b>100.0 / 0.00</b>

Table 4: Generalization to unseen OOD categories across alternative training strategies on the random forests. Point estimates and 95% bootstrap confidence intervals over 100 matched-seed runs are reported.

Strategy	AUROC $\uparrow$				FPR95 % $\downarrow$			
	RSNA PE	MIDRC C19	KiTS	PancreasCT	RSNA PE	MIDRC C19	KiTS	PancreasCT
Dataset-specific	95.80 (92.60–98.50)	93.30 (89.90–96.00)	100.00 (99.90–100.00)	100.00 (100.00–100.00)	15.20 (7.10–23.50)	25.50 (16.80–36.20)	0.10 (0.00–1.00)	0.00 (0.00–0.00)
Ensemble	93.70 (91.70–96.50)	92.80 (89.80–95.60)	100.00 (99.80–100.00)	100.00 (100.00–100.00)	19.90 (11.20–29.10)	32.70 (20.40–54.10)	0.00 (0.00–0.00)	0.00 (0.00–0.00)
Unified	93.00 (85.50–97.50)	91.40 (85.40–94.90)	99.80 (99.00–100.00)	99.90 (99.30–100.00)	24.10 (11.20–42.90)	37.30 (20.90–69.40)	0.70 (0.00–5.60)	0.50 (0.00–4.10)
LODO	91.20 (85.50–95.30)	91.00 (84.40–94.80)	99.80 (99.30–100.00)	100.00 (99.70–100.00)	25.70 (17.30–36.70)	43.20 (23.50–54.10)	0.70 (0.00–4.10)	0.20 (0.00–2.00)
LODO+	92.10 (87.50–95.30)	91.80 (84.40–94.80)	99.80 (99.30–100.00)	100.00 (99.70–100.00)	21.70 (15.30–28.70)	34.20 (25.50–48.10)	0.70 (0.00–4.10)	0.20 (0.00–2.00)

#### 5.4.2. Generalization to unseen OOD categories

We evaluated RF-Deep’s ability to generalize to previously unseen OOD categories using four additional training strategies (Table 4): (i) dataset-specific (DS; default), (ii) ensemble, (iii) unified, (iv) leave-one-dataset-out (LODO), and LODO+. DS trained a separate RF classifier for each OOD dataset, representing an upper-bound setting where the OOD type was known during development and evaluation. Ensemble trained the same four dataset-specific classifiers but averaged their predictions at test time, assuming no knowledge of the test domain during testing. Unified replaced the per-dataset training with a single RF classifier trained on ID versus all OOD datasets combined. LODO followed the standard OOD paradigm by training on ID plus three OOD datasets and evaluating on the held-out fourth, directly measuring generalization to novel OODs. Finally, LODO+ extended LODO by incorporating sub-sampled, non-tumor-centric ROIs to increase anatomical diversity during training.

Performance patterns on near-OOD datasets (RSNA PE and MIDRC C19) revealed important insights on within-anatomy generalization. The LODO strategy showed notable degradation compared to the dataset-specific baseline (RSNA PE: AUROC 91.20 vs 95.80, FPR95 25.70% vs 15.20%; MIDRC C19: AUROC 91.00 vs 93.30, FPR95 43.20% vs. 25.50%). This indicates that training on a single thoracic pathology provides insufficient diversity to generalize to pathologies occurring in the same anatomy. However, LODO+ improved performance over standard LODO (RSNA PE: FPR95 21.70% vs. 25.70%; MIDRC C19: FPR95 34.20% vs. 43.20%), demonstrating that increasing anatomical sampling diversity during training enhanced generalization to unseen near-OOD categories, which is critical for robust OOD detection.

The unified approach, which trained on all thoracic pathologies simultaneously, achieved intermediate performance between LODO and dataset-specific settings (RSNA PE: AUROC 93.00, MIDRC C19: AUROC 91.40), confirming that exposure to multiple within-anatomy pathologies during training improves cross-generalization within the same anatomical region. The ensemble strategy further improved near-OOD performance, approaching dataset-specific performance while maintaining the ability to detect novel OOD categories without prior knowledge of the test

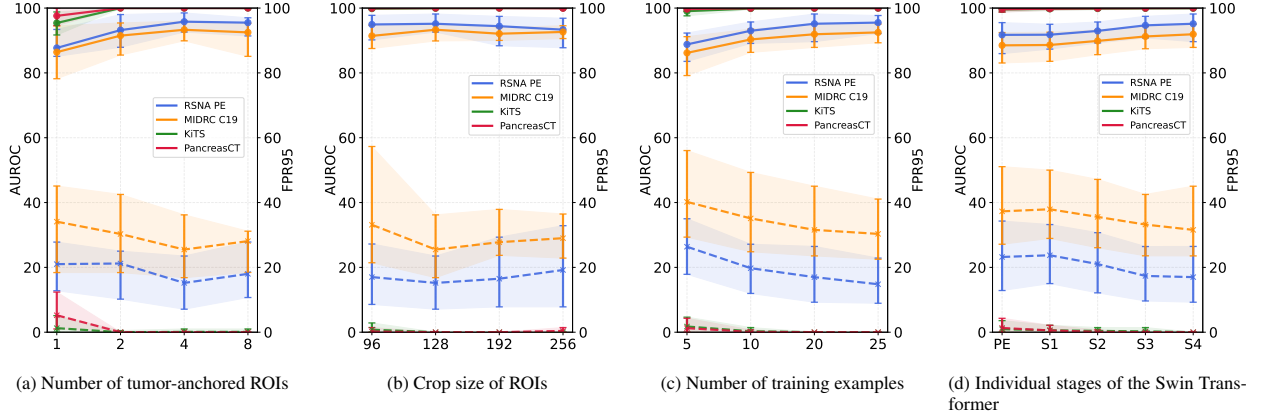


Figure 9: Ablation studies showing the sensitivity of RF-Deep for OOD detection across four datasets. Point estimates and 95% bootstrap confidence intervals over 100 runs with matched seeds are displayed.

domain. On far-OOD datasets (KiTS and PancreasCT), all strategies achieved near-perfect performance ( $\text{AUROC} \geq 99.80$ ,  $\text{FPR95} \leq 0.70\%$ ), with minimal degradation from the dataset-specific baseline.

### 5.5. Design choices and sensitivity analysis

To understand the design choices of our proposed OOD detector, we conducted a series of controlled ablations on the number of ROIs, their crop sizes, the extent of labeled (supervised) data, and the encoder stages used for feature extraction. Figure 9a shows that OOD detection benefits from richer local context around predicted tumor regions, but only up to a point. With  $n = 1$ , performance is unstable, reflected in wider confidence intervals and elevated FPR95, suggesting that a single tumor-anchored crop may miss informative variation in tumor surroundings. Increasing the number of ROIs from one to four improved performance on near-OOD cases, indicating that additional samples may better disambiguate similarly appearing tumor (ID) from non-cancerous structures. Beyond four ROIs, gains plateau and in some cases regress (e.g., MIDRC C19), implying diminishing returns and potential noise injection from redundant or low-value ROIs. Far-OOD datasets did not exhibit performance gains with increasing number of ROIs. Therefore, we used  $n = 4$  to capture meaningful contextual diversity while maintaining computational efficiency.

Figure 9b analyzes the effect of tumor-anchored 3D crop size on OOD detection performance. Performance remained relatively stable on the far-OOD cohorts across crop sizes, with slight preference for  $128 \times 128 \times 128$ . On the near-OOD cohorts, both smaller ( $< 128$ ) and larger ( $> 128$ ) ROIs led to performance degradation, suggesting that the optimal contextual window balances tumor-centered information with surrounding anatomical context.

Figure 9c shows that RF-Deep’s OOD detection performance improved with the number of labeled examples, using equal numbers of ID and OOD scans (5/5, 10/10, up to 20/20, corresponding to less than 30% of available data), after which performance plateaued. With only 20 ID and 20 OOD labeled scans, RF-Deep achieved  $\text{AUROC} > 90$  and  $\text{FPR95} < 30\%$  on average across all OOD datasets. Performance gains were more noticeable on the near-OOD cohorts than the far-OOD cohorts, indicating that detection on subtle shifts in the same anatomical region is trickier and requires more examples than larger shifts across different anatomical regions. Variance decreases consistently as more samples are added, with the strongest variance reduction observed on near-OOD cohorts.

Figure 9d shows individual Swin Transformer stage contributions. Far-OOD cohorts were relatively insensitive to individual stage selection (achieving  $\text{AUROC} > 98$  even when using features from a single stage), whereas the near-OOD counterparts showed strong sensitivity to early stages, with Stage 1 and Stage 2 features being particularly important ( $\text{AUROC} \approx 88\text{--}90$  individually). Concatenating features across all stages yielded the best performance, confirming that hierarchical representations are essential for robust OOD detection. This finding aligns with the SHAP analysis (Section 5.3.2), which showed that RF-Deep adaptively leverages features from different abstraction levels depending on the OOD scenario.

## 6. Discussion

We introduced a lightweight approach for instance-level OOD detection for lung tumor segmentation involving near-OOD and far-OOD cases. Our approach, termed RF-Deep, leveraged the advantage of SSL pretrained transformer encoders to extract image acquisition robust features, while using RF’s feature selection strategy to extract representations that distinguished subtle differences in pathologies occurring in the same disease site as the task model. Our approach improved performance over multiple current OOD detection methods as well as handcrafted radiomics-based RF classifiers under all evaluated datasets. We also found that RF-Deep approach was agnostic to the choice of pretraining approach as well as model size, thus providing a plug-and-play approach for leveraging an existing task-specific DL method for OOD detection.

Analysis of why RF-Deep outperformed other methods showed improved separability of ID from OOD datasets using deep compared to handcrafted radiomic features. Importantly, despite using the same deep features, Mahalanobis distance-based approach was less accurate than RF-Deep, indicating the need for outlier exposure and feature selection performed with random forests to extract a robust non-linear decision boundary. RF-Deep improved over logits-based methods, indicating that over-reliance on the ID model to extract confidence boundaries may be unreliable in OOD scans. Although this issue could be addressed to an extent through confidence calibration, prior studies show limitations of such methods (Larrazabal et al., 2023; Mehrtash et al., 2020).

Our approach has a few limitations. First, RF-Deep performs OOD detection only in scans where a segmentation was generated. Reduction of missing segmentations on ID scans is an altogether different problem and beyond scope of this work. Second, our approach was applied to binary tumor segmentation tasks. Extension to multi-class segmentation, with richer datasets, is straightforward and left for future work. Finally, the evaluated OOD datasets captured some of the key failure modes, but covering all possible pathologies is impractical due to lack of such datasets. Methodologies including continual learning with aggressive data augmentation for incorporating newly discovered failure modes are the next area of development.

## 7. Conclusion

We introduced RF-Deep, a post-hoc out-of-distribution (OOD) detection framework for segmentation models that leverages hierarchical encoder features and random forest classifiers to identify concept drifts. Across near-OOD and far-OOD cohorts, RF-Deep consistently outperformed logit-based methods and radiomics feature-based classifiers. The method is practical as it seamlessly integrates into existing segmentation pipelines without any modification, works across different pretraining strategies and architectures, and provides interpretable predictions through feature attribution.

## Acknowledgment

This research was partially supported by the NCI R01CA258821 and the Memorial Sloan Kettering Cancer Center Support Grant/Core Grant NCI P30CA008748.

## Appendix A. Pretraining strategies descriptions

SMIT (Jiang et al., 2022) consists of masked voxel token prediction, masked patch token distillation, and image token distillation. Masked voxel token prediction is a dense regression task of the intensities within masked patches and is optimized by minimizing the  $\ell_1$  norm between the predicted and ground-truth patches, akin to SimMIM (Xie et al., 2022). Self-distillation (Tarvainen and Valpola, 2017) was required for the next two tasks and was performed using an exponentially moving average (EMA) teacher model with identical architecture as the student, similar to iBOT (Zhou et al., 2022). Masked patch token distillation aligns the voxel token representations learned by the student with those extracted by the teacher from unmasked sequences, optimized with a temperature-scaled cross-entropy loss. For image token distillation, the cross-entropy between global volume embeddings of the student and teacher was minimized. After pretraining, the teacher was discarded and the student encoder was retained for fine-tuning.

Similarly, Swin UNETR (Tang et al., 2022) employs three pretraining tasks. The primary pretext task is masked volume reconstruction, where a proportion of 3D input patches are randomly masked and the model is trained to regress their voxel intensities from visible context. Unlike SimMIM, which leverages positional encodings to aid masked token prediction, this reconstruction task provided no explicit positional information, forcing the model to learn semantically plausible inpainting from local context. 3D rotation prediction enforces invariance by classifying the degree of rotation applied along the z-axis. Finally, contrastive coding encouraged representation learning by maximizing cosine similarity between augmented views of the same volume while minimizing similarity for different volumes. Unlike SMIT, which requires an EMA teacher, Swin UNETR used only a student model. The pretrained encoder was directly retained for fine-tuning.

## Appendix B. Logit-based approaches formulae

The tumor segmentation problem can be broken down into a per-voxel binary classification problem, in which we mean-aggregate the scores of the positive class to summarize the scan. In-distribution (ID) scans tended to yield more confident outputs, whereas out-of-distribution (OOD) scans produced less confident or spurious predictions. Following the convention of treating OOD as the positive class (Hendrycks and Gimpel, 2017; Choi et al., 2024), we negated each score so that higher values correspond to greater likelihood of being OOD. Let  $f^i(x)$  denote the logit for class  $i \in \{0, 1\}$  at voxel  $x$ , and define the softmax score as

$$S_{\text{softmax}}^i(x) = \frac{\exp(f^i(x))}{\sum_{j=0}^1 \exp(f^j(x))}.$$

We denote the set of voxels predicted as positive (tumor) by

$$V_+ = \{(h, w, d) \mid \hat{y}_{h,w,d} = 1\},$$

where  $\hat{y}_{h,w,d}$  is the class prediction at voxel  $(h, w, d)$ . Each logit-based score aggregates over  $V_+$ :

- **MaxSoftmax** (Hendrycks and Gimpel, 2017):

$$S = -\frac{1}{|V_+|} \sum_{(h,w,d) \in V_+} S_{\text{softmax}}^1(x_{h,w,d}).$$

- **MaxLogit** (Hendrycks et al., 2022):

$$S = -\frac{1}{|V_+|} \sum_{(h,w,d) \in V_+} f^1(x_{h,w,d}).$$

- **Energy** (Liu et al., 2020):

$$S = -\frac{1}{|V_+|} \sum_{(h,w,d) \in V_+} \log\left(\sum_{i=0}^1 \exp(f^i(x_{h,w,d}))\right).$$

## Appendix C. Additional results

This section provides additional quantitative and qualitative results that support the findings presented in the paper.

- Figure C.10 presents the disaggregated analysis of segmentation performance across imaging variations, discussed briefly in Section 5.1 (Figure 3).
- Table C.5 lists the mapping from feature IDs used across Sections 5.2 and 5.3 to standardized IBSI feature names (retaining only those post recursive feature elimination).

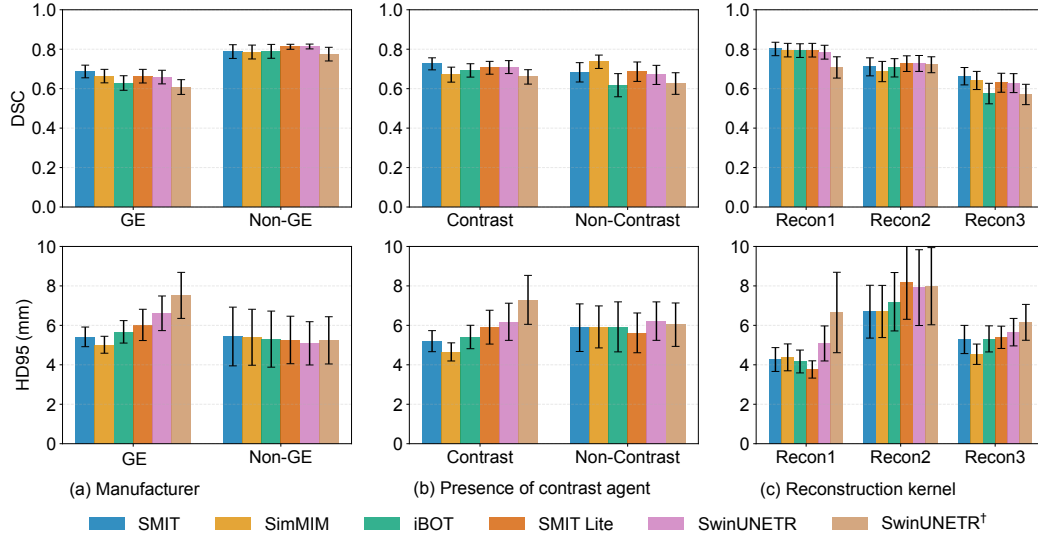


Figure C.10: Segmentation performance across backbones under imaging variations (scanner type, contrast, reconstruction kernel) on the ID dataset. DSC and HD95 are reported.

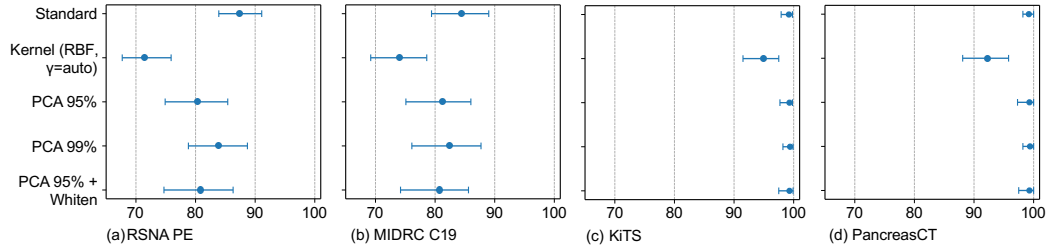


Figure C.11: Ablation of Mahalanobis distance-based variants for OOD detection using AUROC over 100 matched-seed runs.

- Figure C.11 supports the discussion in Section 5.2 on MD-Deep, demonstrating that the standard formulation outperforms all variants.
- Table C.6 reports the complete OOD detection performance of RF-Deep across all six evaluated backbones, briefly discussed in Section 5.2.
- Table C.7 summarizes OOD performance for all methods (five additional pretraining strategies on six methods), reinforcing the findings in Section 5.2.
- Figure C.12 shows t-SNE embeddings for all alternative pretraining strategies, complementing Figure 4a and discussions in Sections 5.2 and 5.3.1.

## References

- Aerts, H.J.W.L., Velazquez, E.R., Leijenaar, R.T.H., Parmar, C., Grossmann, P., Cavalho, S., Bussink, J., Monshouwer, R., Haibe-Kains, B., Rietveld, D., et al., 2015. Data from nsclc-radiomics. The cancer imaging archive .
- Apte, A.P., Iyer, A., Crispin-Ortuzar, M., Pandya, R., Van Dijk, L.V., Spezi, E., Thor, M., Um, H., Veeraraghavan, H., Oh, J.H., et al., 2018. Extension of CERR for computational radiomics: A comprehensive MATLAB platform for reproducible radiomics research. Medical physics .

Table C.5: Radiomics features definitions.

ID	Feature	ID	Feature
<i>General features</i>			
<i>feat_5</i>	maxIntensityInterpReseg	<i>feat_6</i>	minIntensityInterpReseg
<i>Shape features</i>			
<i>shape_7</i>	max2dDiameterSagittalPlane	<i>shape_11</i>	volume
<i>shape_12</i>	filledVolume	<i>shape_18</i>	surfToVolRatio
<i>First-order features</i>			
<i>first_1</i>	min	<i>first_2</i>	max
<i>first_4</i>	range	<i>first_10</i>	entropy
<i>first_12</i>	energy	<i>first_13</i>	totalEnergy
<i>Gray-Level Co-occurrence Matrix (GLCM) features</i>			
<i>glcm_8</i>	jointEntropy_3D_StdDev	<i>glcm_18</i>	jointAvg_3D_StdDev
<i>glcm_36</i>	sumEntropy_3D_avg	<i>glcm_37</i>	sumEntropy_3D_Median
<i>glcm_39</i>	sumEntropy_3D_Min	<i>glcm_43</i>	contrast_3D_StdDev
<i>glcm_44</i>	contrast_3D_Min	<i>glcm_47</i>	invDiffMom_3D_Median
<i>glcm_48</i>	invDiffMom_3D_StdDev	<i>glcm_58</i>	invDiff_3D_StdDev
<i>glcm_59</i>	invDiff_3D_Min	<i>glcm_60</i>	invDiff_3D_Max
<i>glcm_61</i>	invDiffNorm_3D_avg	<i>glcm_63</i>	invDiffNorm_3D_StdDev
<i>glcm_68</i>	invVar_3D_StdDev	<i>glcm_76</i>	diffEntropy_3D_avg
<i>glcm_77</i>	diffEntropy_3D_Median	<i>glcm_78</i>	diffEntropy_3D_StdDev
<i>glcm_79</i>	diffEntropy_3D_Min	<i>glcm_80</i>	diffEntropy_3D_Max
<i>glcm_81</i>	diffVar_3D_avg	<i>glcm_82</i>	diffVar_3D_Median
<i>glcm_84</i>	diffVar_3D_Min	<i>glcm_89</i>	diffAvg_3D_Min
<i>glcm_92</i>	corr_3D_Median	<i>glcm_93</i>	corr_3D_StdDev
<i>glcm_95</i>	corr_3D_Max	<i>glcm_98</i>	clustTendency_3D_StdDev
<i>Gray-Level Run-Length Matrix (GLRLM) features</i>			
<i>glrlm_28</i>	runLengthNonUniformityNorm_3D_StdDev	<i>glrlm_68</i>	grayLevelVariance_3D_StdDev
<i>glrlm_73</i>	runLengthVariance_3D_StdDev	<i>glrlm_78</i>	runEntropy_3D_StdDev
<i>Gray-Level Size Zone Matrix (GLSZM) features</i>			
<i>glszm_3</i>	grayLevelNonUniformity_3D		
<i>Gray-Tone Difference Matrix (GTDM) features</i>			
<i>gtdm_5</i>	strength_3D		

Araujo, T., Aresta, G., Schmidt-Erfurth, U., Bogunović, H., 2023. Few-shot out-of-distribution detection for automated screening in retinal oct images using deep learning. Scientific Reports .

Azizi, S., Culp, L., Freyberg, J., Mustafa, B., Baur, S., Kornblith, S., Chen, T., Tomasev, N., Mitrović, J., Strachan, P., Mahdavi, S.S., Wulczyn, E., Babenko, B., Walker, M., Loh, A., Chen, P.H.C., Liu, Y., Bavishi, P., McKinney, S.M., Winkens, J., Roy, A.G., Beaver, Z., Ryan, F., Krogue, J., Etemadi, M., Telang, U., Liu, Y., Peng, L., Corrado, G.S., Webster, D.R., Fleet, D., Hinton, G., Houlby, N., Karthikesalingam, A., Norouzi, M., Natarajan, V., 2023. Robust and data-efficient generalization of self-supervised machine learning for diagnostic imaging. Nature Biomedical Engineering .

Bakr, S., Gevaert, O., Echegaray, S., Ayers, K., Zhou, M., Shafiq, M., Zheng, H., Zhang, W., Leung, A., Kadoch, M., et al., 2017. Data for nscl radiogenomics collection. The Cancer Imaging Archive .

Banerjee, I., Bhattacharjee, K., Burns, J.L., Trivedi, H., Purkayastha, S., Seyyed-Kalantari, L., Patel, B.N., Shirad-

Table C.6: RF-Deep OOD detection performance across different backbone encoders. AUROC ( $\uparrow$ ) and FPR95 ( $\downarrow$ ) with 95% bootstrap confidence intervals are reported over 100 matched-seed runs.

Backbone	RSNA PE		MIDRC C19		KiTS		PancreasCT	
	AUROC	FPR95 %	AUROC	FPR95 %	AUROC	FPR95 %	AUROC	FPR95 %
SimMIM	93.70 (90.40–96.10)	17.60 (10.20–28.10)	93.20 (90.10–96.10)	26.50 (18.30–38.20)	99.90 (99.80–100.00)	0.10 (0.00–1.00)	99.90 (99.80–100.00)	0.60 (0.00–2.00)
iBOT	93.60 (91.70–96.80)	22.60 (12.20–42.40)	92.70 (89.30–96.30)	24.60 (14.70–36.70)	99.80 (99.30–100.00)	1.10 (0.00–4.10)	99.80 (98.90–100.00)	1.10 (0.00–7.70)
SMIT Lite	94.10 (90.10–96.10)	20.40 (11.20–34.30)	90.40 (86.70–94.10)	30.50 (20.40–41.80)	99.60 (99.30–99.90)	1.80 (0.50–3.10)	99.30 (98.80–99.90)	1.80 (0.00–4.10)
Swin UNETR	89.60 (85.10–92.90)	34.10 (20.40–51.10)	88.90 (84.70–92.20)	37.50 (25.00–52.60)	99.70 (99.20–99.90)	2.40 (0.00–5.10)	99.60 (99.00–99.90)	2.90 (0.00–6.10)
Swin UNETR <sup>†</sup>	90.40 (84.70–94.10)	41.50 (25.00–58.20)	88.60 (83.50–92.30)	35.80 (24.50–50.00)	99.40 (98.60–99.90)	2.60 (0.00–6.10)	98.70 (97.00–99.80)	7.10 (1.00–18.90)
SMIT	95.80 (92.60–98.50)	15.20 (7.10–23.50)	93.30 (89.90–96.00)	25.50 (16.80–36.20)	100.00 (99.90–100.00)	0.10 (0.00–1.00)	100.00 (100.00–100.00)	0.00 (0.00–0.00)

- kar, R., Gichoya, J., 2023. “Shortcuts” causing bias in radiology artificial intelligence: causes, evaluation, and mitigation. *Journal of the American College of Radiology* .
- Berger, C., Paschali, M., Glocker, B., Kamnitsas, K., 2021. Confidence-based out-of-distribution detection: a comparative study and analysis, in: *International Workshop on Uncertainty for Safe Utilization of Machine Learning in Medical Imaging*, Springer. pp. 122–132.
- Biase, A.D., Ziegfeld, L., Sijtsma, N.M., Steenbakkers, R., Wijsman, R., van Dijk, L.V., Langendijk, J.A., Cnossen, F., van Ooijen, P.M.A., 2024. Probability maps for deep learning-based head and neck tumour segmentation: Graphical user interface design and test. *Computers in Biology and Medicine* .
- Boone, L., Biparva, M., Mojiri Forooshani, P., Ramirez, J., Masellis, M., Bartha, R., Symons, S., Strother, S., Black, S.E., Heyn, C., Martel, A.L., Swartz, R.H., Goubran, M., 2023. Rood-mri: Benchmarking the robustness of deep learning segmentation models to out-of-distribution and corrupted data in mri. *NeuroImage* .
- Budzyń, K., Romańczyk, M., Kitala, D., Kołodziej, P., Bugajski, M., Adami, H.O., Blom, J., Buszkiewicz, M., Halvorsen, N., Hassan, C., Romańczyk, T., Holme, Ø., Jarus, K., Fielding, S., Kunar, M., Pellise, M., Pilonis, N., Kamiński, M.F., Kalager, M., Bretthauer, M., Mori, Y., 2025. Endoscopist deskillng risk after exposure to artificial intelligence in colonoscopy: a multicentre, observational study. *The Lancet Gastroenterology & Hepatology* .
- Cardoso, M.J., Li, W., Brown, R., Ma, N., Kerfoot, E., Wang, Y., Murrey, B., Myronenko, A., Zhao, C., Yang, D., et al., 2022. MONAI: An open-source framework for deep learning in healthcare. *arXiv preprint arXiv:2211.02701* .
- Chen, C., Qin, C., Ouyang, C., Li, Z., Wang, S., 2022. Enhancing mr image segmentation with realistic adversarial data augmentation. *Medical Image Analysis* .
- Choi, C., Tajwar, F., Lee, Y., Yao, H., Kumar, A., Finn, C., 2024. Conservative prediction via data-driven confidence minimization. *Transactions on Machine Learning Research* .
- Colak, E., Kitamura, F.C., Hobbs, S.B., Wu, C.C., Lungren, M.P., Prevedello, L.M., Kalpathy-Cramer, J., Ball, R.L., Shih, G., Stein, A., et al., 2021. The rsna pulmonary embolism ct dataset. *Radiology: Artificial Intelligence* .
- Davis, J., Goadrich, M., 2006. The relationship between precision-recall and roc curves, in: *Proceedings of the 23rd international conference on Machine learning*, pp. 233–240.
- Du, Y., Bai, F., Huang, T., Zhao, B., 2024. SegVol: Universal and interactive volumetric medical image segmentation, in: *Advances in Neural Information Processing Systems*, Curran Associates, Inc.. pp. 110746–110783.

Table C.7: RF-Deep OOD detection performance across different pretrained backbone encoders. AUROC ( $\uparrow$ ) and FPR95 ( $\downarrow$ ) with 95% bootstrap confidence intervals are reported over 100 matched-seed runs.

Model	Method	RSNA PE		MIDRC C19		KiTS		PancreasCT	
		AUROC	FPR95 %	AUROC	FPR95 %	AUROC	FPR95 %	AUROC	FPR95 %
SimMIM	MaxSoftmax	86.89	45.56	84.58	54.92	94.19	21.59	94.30	24.04
	MaxLogit	89.39	44.04	87.55	45.65	95.99	15.32	96.28	14.82
	Energy	89.70	44.64	87.75	45.24	96.15	14.92	96.39	13.84
	RF-Radiomics	87.20	48.90	89.80	34.90	97.00	15.80	96.60	17.90
	MD-Deep	88.60	41.32	86.85	51.72	97.66	3.40	97.84	8.30
	RF-Deep	93.70	17.60	93.20	26.50	99.90	0.10	99.90	0.60
iBOT	MaxSoftmax	83.56	48.25	80.97	52.10	90.45	32.22	88.98	36.23
	MaxLogit	87.31	38.55	85.24	39.33	93.82	23.45	92.29	27.17
	Energy	87.90	38.62	85.84	39.61	94.49	22.02	92.96	25.17
	RF-Radiomics	89.30	50.90	90.50	29.70	96.80	14.70	96.80	15.20
	MD-Deep	87.83	44.87	86.12	52.89	98.63	6.62	96.16	17.27
	RF-Deep	93.60	22.60	92.70	24.60	99.80	1.10	99.80	1.10
SMIT Lite	MaxSoftmax	77.96	56.05	74.44	60.96	80.77	48.42	87.35	41.45
	MaxLogit	78.52	53.32	79.03	51.95	79.46	45.97	85.42	41.33
	Energy	78.16	53.82	79.37	52.22	78.74	45.59	83.90	40.53
	RF-Radiomics	88.90	38.90	90.70	31.10	97.10	13.80	97.40	12.80
	MD-Deep	85.94	38.85	78.51	56.77	93.51	25.57	92.26	25.06
	RF-Deep	94.10	20.40	90.40	30.50	99.60	1.80	99.30	1.80
Swin UNETR	MaxSoftmax	80.30	52.19	79.65	62.01	84.40	46.38	88.97	46.98
	MaxLogit	83.88	42.62	83.85	52.12	88.99	34.86	91.57	35.45
	Energy	84.16	40.77	84.30	50.44	89.41	31.86	92.17	33.91
	RF-Radiomics	87.70	37.40	89.20	33.40	98.10	9.80	98.10	13.70
	MD-Deep	77.88	62.47	74.14	64.61	92.61	25.50	89.54	29.67
	RF-Deep	89.60	34.10	88.90	37.50	99.70	2.40	99.60	2.90
Swin UNETR <sup>†</sup>	MaxSoftmax	75.92	53.25	77.83	55.91	78.89	53.17	93.12	23.96
	MaxLogit	77.87	43.65	80.41	49.93	83.33	39.30	92.37	18.44
	Energy	78.02	42.46	80.78	49.48	83.87	38.24	92.17	18.98
	MD-Deep	74.03	68.07	70.50	71.02	84.56	49.44	79.45	63.34
	RF-Radiomics	86.50	40.00	89.00	37.20	97.40	11.30	97.80	11.70
	RF-Deep	90.40	41.50	88.60	35.80	99.40	2.60	98.70	7.10

Fedorov, A., Geenjaar, E., Wu, L., DeRamus, T.P., Calhoun, V.D., Plis, S.M., 2021. Tasting the cake: Evaluating self-supervised generalization on out-of-distribution multimodal mri data, in: ICLR 2021 Workshop on RobustML. Presented at RobustML workshop at ICLR 2021.

Gao, L., Wu, S., 2020. Response score of deep learning for out-of-distribution sample detection of medical images. Journal of biomedical informatics .

Godau, P., Kalinowski, P., Christodoulou, E., Reinke, A., Tizabi, M., Ferrer, L., Jäger, P., Maier-Hein, L., 2025. Navigating prevalence shifts in image analysis algorithm deployment. Medical Image Analysis .

Goddard, K., Roudsari, A., Wyatt, J.C., 2012. Automation bias: a systematic review of frequency, effect mediators, and mitigators. Journal of the American Medical Informatics Association .

Gomez, J.T., Rangnekar, A., Williams, H., Thompson, H., Garcia-Aguilar, J., Smith, J.J., Veeraraghavan, H., 2025. Swin transformers are robust to distribution and concept drift in endoscopy-based longitudinal rectal cancer assessment, in: Proc. SPIE 13406, Medical Imaging 2025: Image Processing, 134061N.

González, C., Gotkowski, K., Fuchs, M., Bucher, A., Dadras, A., Fischbach, R., Kaltenborn, I.J., Mukhopadhyay, A., 2022. Distance-based detection of out-of-distribution silent failures for covid-19 lung lesion segmentation. Medical image analysis .

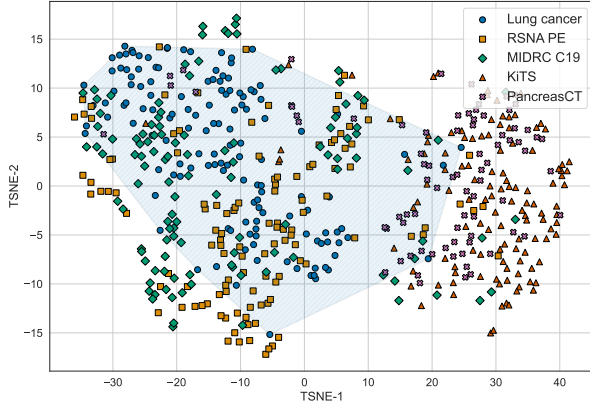
- Graham, M.S., Pinaya, W.H.L., Wright, P., Tudosiu, P.D., Mah, Y.H., Teo, J.T., Jäger, H.R., Werring, D., Nachev, P., Ourselin, S., et al., 2023. Unsupervised 3d out-of-distribution detection with latent diffusion models, in: International Conference on Medical Image Computing and Computer-Assisted Intervention, Springer.
- Gu, H., Dong, H., Yang, J., Mazurowski, M.A., 2025. How to build the best medical image segmentation algorithm using foundation models: a comprehensive empirical study with segment anything model. *Machine Learning for Biomedical Imaging*.
- Gu, R., Zhang, J., Huang, R., Lei, W., Wang, G., Zhang, S., 2021. Domain composition and attention for unseen-domain generalizable medical image segmentation, in: Proceedings of the 24th International Conference on Medical Image Computing and Computer Assisted Intervention (MICCAI 2021), Springer.
- Guha Roy, A., Ren, J., Azizi, S., Loh, A., Natarajan, V., Mustafa, B., Pawlowski, N., Freyberg, J., Liu, Y., Beaver, Z., Vo, N., Bui, P., Winter, S., MacWilliams, P., Corrado, G.S., Telang, U., Liu, Y., Cemgil, T., Karthikesalingam, A., Lakshminarayanan, B., Winkens, J., 2022. Does your dermatology classifier know what it doesn't know? detecting the long-tail of unseen conditions. *Medical Image Analysis*.
- Haghighi, F., Taher, M.R.H., Gotway, M.B., Liang, J., 2022. DiRA: discriminative, restorative, and adversarial learning for self-supervised medical image analysis, in: Proceedings of the IEEE/CVF Conference on Computer Vision and Pattern Recognition.
- Hatamizadeh, A., Nath, V., Tang, Y., Yang, D., Roth, H.R., Xu, D., 2022. Swin UNETR: Swin transformers for semantic segmentation of brain tumors in mri images, in: Brainlesion: Glioma, Multiple Sclerosis, Stroke and Traumatic Brain Injuries, Springer International Publishing, Cham.
- He, K., Chen, X., Xie, S., Li, Y., Doll'ar, P., Girshick, R.B., 2021. Masked autoencoders are scalable vision learners. 2022 ieee, in: CVF Conference on Computer Vision and Pattern Recognition (CVPR).
- Heller, N., Isensee, F., Trofimova, D., Tejpaul, R., Zhao, Z., Chen, H., Wang, L., Golts, A., Khapun, D., Shats, D., Shoshan, Y., Gilboa-Solomon, F., George, Y., Yang, X., Zhang, J., Zhang, J., Xia, Y., Wu, M., Liu, Z., Walczak, E., McSweeney, S., Vasdev, R., Hornung, C., Solaiman, R., Schoepfoerster, J., Abernathy, B., Wu, D., Abdulkadir, S., Byun, B., Spriggs, J., Struyk, G., Austin, A., Simpson, B., Hagstrom, M., Virnig, S., French, J., Venkatesh, N., Chan, S., Moore, K., Jacobsen, A., Austin, S., Austin, M., Regmi, S., Papanikolopoulos, N., Weight, C., 2023. The KiTS21 challenge: Automatic segmentation of kidneys, renal tumors, and renal cysts in corticomedullary-phase ct. *arXiv:2307.01984*.
- Hendrycks, D., Basart, S., Mazeika, M., Zou, A., Mostajabi, M., Steinhardt, J., Song, D.X., 2022. Scaling out-of-distribution detection for real-world settings, in: International Conference on Machine Learning.
- Hendrycks, D., Gimpel, K., 2017. A baseline for detecting misclassified and out-of-distribution examples in neural networks. *Proceedings of International Conference on Learning Representations*.
- Hendrycks, D., Mazeika, M., Dietterich, T., 2019. Deep anomaly detection with outlier exposure. *Proceedings of the International Conference on Learning Representations*.
- Huang, S., Chaudhari, A.S., Langlotz, C.P., Shah, N., Yeung, S., Lungren, M.P., 2022. Developing medical imaging ai for emerging infectious diseases. *Nature Communications*.
- Humblot-Renaux, G., Escalera, S., Moeslund, T.B., 2023. Beyond auroc & co. for evaluating out-of-distribution detection performance, in: Proceedings of the IEEE/CVF Conference on Computer Vision and Pattern Recognition.
- Jiang, J., Rangnekar, A., Veeraraghavan, H., 2024. Self-supervised learning improves robustness of deep learning lung tumor segmentation models to ct imaging differences. *Medical Physics*.
- Jiang, J., Tyagi, N., Tringale, K., Crane, C., Veeraraghavan, H., 2022. Self-supervised 3d anatomy segmentation using self-distilled masked image transformer (SMIT), in: International Conference on Medical Image Computing and Computer-Assisted Intervention, Springer.

- Jung, W., Park, S., Jung, K.H., Hwang, S.I., 2019. Prostate cancer segmentation using manifold mixup u-net, in: Proceedings of the MIDL Workshop / Extended Abstracts, London, UK.
- Karimi, D., Gholipour, A., 2022. Improving calibration and out-of-distribution detection in deep models for medical image segmentation. *IEEE transactions on artificial intelligence* .
- Koch, L., Baumgartner, C., Berens, P., 2024. Distribution shift detection for the postmarket surveillance of medical AI algorithms: a retrospective simulation study. *NPJ Digital Medicine* .
- Konz, N., Chen, Y., Gu, H., Dong, H., Chen, Y., Mazurowski, M.A., 2024. RaD: A metric for medical image distribution comparison in out-of-domain detection and other applications. *arXiv preprint 2412.01496* .
- Larrazabal, A.J., Martinez, C., Dolz, J., Ferrante, E., 2023. Maximum entropy on erroneous predictions: Improving model calibration for medical image segmentation, in: *Medical Image Computing and Computer Assisted Intervention – MICCAI 2023*, Springer Cham. pp. 327–337.
- Lee, K., Lee, K., Lee, H., Shin, J., 2018. A simple unified framework for detecting out-of-distribution samples and adversarial attacks. *Advances in neural information processing systems* .
- Lempart, M., Scherman, J., Nilsson, M.P., Jamtheim Gustafsson, C., 2023. Deep learning-based classification of organs at risk and delineation guideline in pelvic cancer radiation therapy. *Journal of Applied Clinical Medical Physics* .
- Liang, S., Li, Y., Srikant, R., 2018. Enhancing the reliability of out-of-distribution image detection in neural networks, in: *International Conference on Learning Representations (ICLR)*.
- Liu, W., Wang, X., Owens, J., Li, Y., 2020. Energy-based out-of-distribution detection. *Advances in neural information processing systems* .
- Liu, Z., Lin, Y., Cao, Y., Hu, H., Wei, Y., Zhang, Z., Lin, S., Guo, B., 2021. Swin transformer: Hierarchical vision transformer using shifted windows, in: *Proceedings of the IEEE/CVF international conference on computer vision*.
- Lundberg, S.M., Lee, S.I., 2017. A unified approach to interpreting model predictions. *Advances in neural information processing systems* .
- Mehrtash, A., Wells, W.M., Tempany, C.M., Abolmaesumi, P., Kapur, T., 2020. Confidence calibration and predictive uncertainty estimation for deep medical image segmentation. *IEEE transactions on medical imaging* 39, 3868–3878.
- Nalisnick, E.T., Matsukawa, A., Teh, Y.W., Görür, D., Lakshminarayanan, B., 2019. Do deep generative models know what they don’t know?, in: *7th International Conference on Learning Representations, ICLR 2019, New Orleans, LA, USA, May 6-9, 2019*, OpenReview.net.
- Nandy, J., Hs, W., Le, M.L., 2021. Distributional shifts in automated diabetic retinopathy screening, in: *2021 IEEE International Conference on Image Processing (ICIP)*, IEEE.
- Nguyen, D.M.H., Nguyen, H., Mai, T.T.N., Cao, T., Nguyen, B.T., Ho, N., Swoboda, P., Albarqouni, S., Xie, P., Sonntag, D., 2023. Joint self-supervised image-volume representation learning with intra-inter contrastive clustering, in: *Proc. 37th AAAI*, AAAI Press.
- Nguyen, V.P., Trinh, N.H., Nguyen, D.M.L., Nguyen, P.L., Tran, Q.L., 2026. Aleatoric uncertainty medical image segmentation estimation via flow matching, in: *Sudre, C.H., Hoque, M.I., Mehta, R., Ouyang, C., Qin, C., Rakic, M., Wells, W.M. (Eds.), Uncertainty for Safe Utilization of Machine Learning in Medical Imaging*, Springer Nature Switzerland, Cham. pp. 134–144.
- Nichyporuk, B., Cardinell, J., Szeto, J., Mehta, R., Falet, J.P., Arnold, D.L., Tsaftaris, S.A., Arbel, T., 2022. Re-thinking generalization: The impact of annotation style on medical image segmentation. *Machine Learning for Biomedical Imaging* .

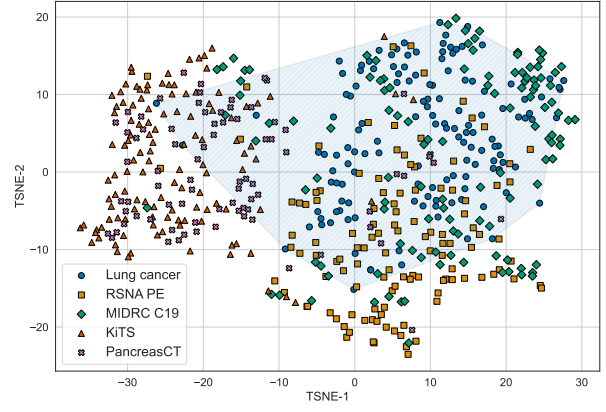
- Otles, E., Oh, J., Li, B., Bochinski, M., Joo, H., Ortwine, J., et al., 2021. Mind the performance gap: Examining dataset shift during prospective validation, in: Ken, J., Serena, Y., Mark, S. (Eds.), *Proceedings of the 6th Machine Learning for Healthcare Conference*, PMLR.
- Panfilov, E., Tiulpin, A., Klein, S., Nieminen, M.T., Saarakkala, S., 2019. Improving robustness of deep learning based knee mri segmentation: Mixup and adversarial domain adaptation, in: *Proceedings of the IEEE/CVF International Conference on Computer Vision Workshops (ICCVW)*, IEEE, Seoul, Korea.
- Paszke, A., Gross, S., Massa, F., Lerer, A., Bradbury, J., Chanan, G., Killeen, T., Lin, Z., Gimelshein, N., Antiga, L., et al., 2019. Pytorch: An imperative style, high-performance deep learning library. *Advances in neural information processing systems* .
- Pinaya, W.H., Tudosiu, P.D., Gray, R., Rees, G., Nachev, P., Ourselin, S., Cardoso, M.J., 2022. Unsupervised brain imaging 3d anomaly detection and segmentation with transformers. *Medical Image Analysis* .
- Prabhu, V., Yenamandra, S., Singh, A., Hoffman, J., 2022. Adapting self-supervised vision transformers by probing attention-conditioned masking consistency. *Advances in neural information processing systems* .
- Qayyum, A., Razzak, I., Mazher, M., Khan, T., Ding, W., Niederer, S., 2023. Two-stage self-supervised contrastive learning aided transformer for real-time medical image segmentation. *IEEE Journal of Biomedical and Health Informatics* .
- Quiñonero-Candela, J., Sugiyama, M., Schwaighofer, A., Lawrence, N.D., 2022. *Dataset shift in machine learning*. Mit Press.
- Rangnekar, A., Nadkarni, N., Jiang, J., Veeraraghavan, H., 2025. Quantifying uncertainty in lung cancer segmentation with foundation models applied to mixed-domain datasets, in: *Proceedings of SPIE — Medical Imaging 2025: Image Processing*, SPIE.
- Ren, J., Teuwen, J., Nijkamp, J., Rasmussen, M., Gouw, Z., Eriksen, J.G., Sonke, J.J., Korreman, S., 2024. Enhancing the reliability of deep learning-based head and neck tumour segmentation using uncertainty estimation with multi-modal images. *Physics in Medicine & Biology* .
- Ronneberger, O., Fischer, P., Brox, T., 2015. U-net: Convolutional networks for biomedical image segmentation, in: *International Conference on Medical Image Computing and Computer-Assisted Intervention*, Springer.
- Roschewitz, M., Khara, G., Yearsley, J., Sharma, N., James, J.J., Éva Ambrózay, Heroux, A., Kecskemethy, P., Rijken, T., Glocker, B., 2023. Automatic correction of performance drift under acquisition shift in medical image classification. *Nature Communications* .
- Roth, H.R., Lu, L., Farag, A., Shin, H.C., Liu, J., Turkbey, E.B., Summers, R.M., 2015. Deeporgan: Multi-level deep convolutional networks for automated pancreas segmentation, in: *Medical Image Computing and Computer-Assisted Intervention—MICCAI 2015: 18th International Conference, Munich, Germany, October 5-9, 2015, Proceedings, Part I* 18, Springer.
- Roy, A.G., Ren, J., Azizi, S., Loh, A., Natarajan, V., Mustafa, B., Pawlowski, N., Freyberg, J., Liu, Y., Beaver, Z., et al., 2022. Does your dermatology classifier know what it doesn't know? detecting the long-tail of unseen conditions. *Medical Image Analysis* .
- Safdari, R., Nikouei Mahani, M.A., Koohi-Moghadam, M., Bae, K.T., 2025. Mixstyleflow: Domain generalization in medical image segmentation using normalizing flows, in: *Proceedings of the 28th International Conference on Medical Image Computing and Computer Assisted Intervention (MICCAI 2025)*, Springer Nature Switzerland.
- Saha, A., Hosseinzadeh, M., Huisman, H., 2021. End-to-end prostate cancer detection in bpmri via 3d cnns: Effects of attention mechanisms, clinical priori and decoupled false positive reduction. *Medical Image Analysis* .

- Sahiner, B., Chen, W., Samala, R.K., Petrick, N., 2023. Data drift in medical machine learning: implications and potential remedies. *The British Journal of Radiology* .
- Simeth, J., Jiang, J., Nosov, A., Wibmer, A., Zelefsky, M., Tyagi, N., Veeraraghavan, H., 2023. Deep learning-based dominant index lesion segmentation for mr-guided radiation therapy of prostate cancer. *Medical Physics* .
- Szyc, K., Walkowiak, T., Maciejewski, H., 2023. Why out-of-distribution detection experiments are not reliable-subtle experimental details muddle the ood detector rankings, in: *Uncertainty in Artificial Intelligence*, PMLR.
- Tang, Y., Yang, D., Li, W., Roth, H.R., Landman, B., Xu, D., Nath, V., Hatamizadeh, A., 2022. Self-supervised pre-training of swin transformers for 3d medical image analysis, in: *Proceedings of the IEEE/CVF Conference on Computer Vision and Pattern Recognition*.
- Tardy, M., Scheffer, B., Mateus, D., 2019. Uncertainty measurements for the reliable classification of mammograms, in: *International conference on medical image computing and computer-assisted intervention*, Springer.
- Tarvainen, A., Valpola, H., 2017. Mean teachers are better role models: Weight-averaged consistency targets improve semi-supervised deep learning results, in: *Proceedings of the 31st International Conference on Neural Information Processing Systems*, Curran Associates Inc.
- Thulasidasan, S., Thapa, S., Dhaubhadel, S., Chennupati, G., Bhattacharya, T., Bilmes, J., 2021. An effective baseline for robustness to distributional shift, in: *2021 20th IEEE International Conference on Machine Learning and Applications (ICMLA)*, IEEE.
- Tsai, E.B., Simpson, S., Lungren, M.P., Hershman, M., Roshkovan, L., Colak, E., Erickson, B.J., Shih, G., Stein, A., Kalpathy-Cramer, J., Shen, J., Hafez, M.A., John, S., Rajiah, P., Pogatchnik, B.P., Mongan, J.T., Altinmakas, E., Ranschaert, E., Kitamura, F.C., Topff, L., Moy, L., Kanne, J.P., Wu, C., 2021. Medical imaging data resource center (MIDRC) - RSNA international COVID open research database (RICORD) release 1b - chest ct covid-.
- Vaish, M., Meister, F., Heimann, T., Brune, C., Wolterink, J.M., 2025. Data-agnostic augmentations for unknown variations: Out-of-distribution generalisation in MRI segmentation, in: *Medical Imaging with Deep Learning*.
- Vasiliuk, A., Frolova, D., Belyaev, M., Shirokikh, B., 2023. Limitations of out-of-distribution detection in 3d medical image segmentation. *Journal of Imaging* .
- Wen, R., Yuan, H., Ni, D., Xiao, W., Wu, Y., 2024. From denoising training to test-time adaptation: Enhancing domain generalization for medical image segmentation, in: *Proceedings of the IEEE/CVF Winter Conference on Applications of Computer Vision (WACV)*, IEEE / Computer Vision Foundation.
- Willeminck, M., Roth, R., Sandfort, V., 2022. Toward foundational deep learning models for medical imaging in the new era of transformer networks. *Radiol Artif Intell* .
- Woodland, M., Patel, N., Castelo, A., Al Taie, M., Eltaher, M., Yung, J.P., Netherton, T.J., Calderone, T.L., Sanchez, J.I., Cleere, D.W., et al., 2024. Dimensionality reduction and nearest neighbors for improving out-of-distribution detection in medical image segmentation. *The journal of machine learning for biomedical imaging* .
- Xie, Z., Zhang, Z., Cao, Y., Lin, Y., Bao, J., Yao, Z., Dai, Q., Hu, H., 2022. Simmim: A simple framework for masked image modeling, in: *Proceedings of the IEEE/CVF conference on computer vision and pattern recognition*.
- Yan, X., Naushad, J., Sun, S., Han, K., Tang, H., Kong, D., Ma, H., You, C., Xie, X., 2023. Representation recovering for self-supervised pre-training on medical images, in: *2023 IEEE/CVF Winter Conference on Applications of Computer Vision (WACV)*.
- Yuan, M., Xia, Y., Dong, H., Chen, Z., Yao, J., Qiu, M., Yan, K., Yin, X., Shi, Y., Chen, X., et al., 2023. Devil is in the queries: Advancing mask transformers for real-world medical image segmentation and out-of-distribution localization, in: *Proceedings of the IEEE/CVF Conference on Computer Vision and Pattern Recognition*.

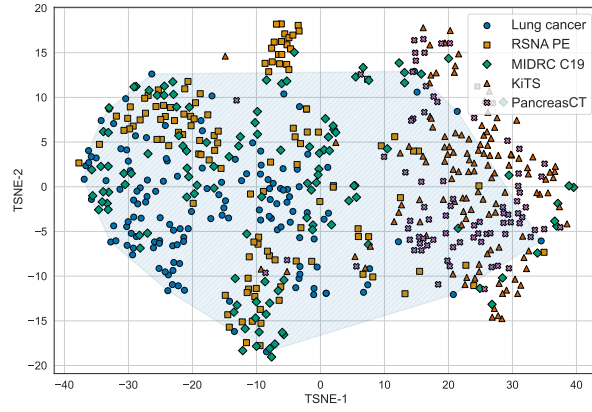
- Zhou, J., Wei, C., Wang, H., Shen, W., Xie, C., Yuille, A., Kong, T., 2022. iBOT: Image bert pre-training with online tokenizer. International Conference on Learning Representations (ICLR) .
- Zwanenburg, A., Vallières, M., Abdalah, M.A., Aerts, H.J., Andrearczyk, V., Apte, A., Ashrafinia, S., Bakas, S., Beukinga, R.J., Boellaard, R., et al., 2020. The image biomarker standardization initiative: standardized quantitative radiomics for high-throughput image-based phenotyping. Radiology .



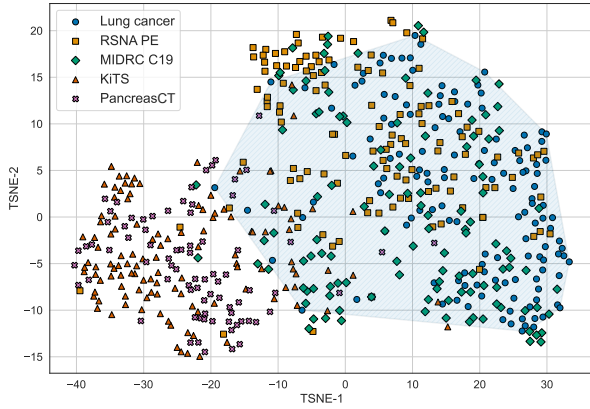
(a) SimMIM



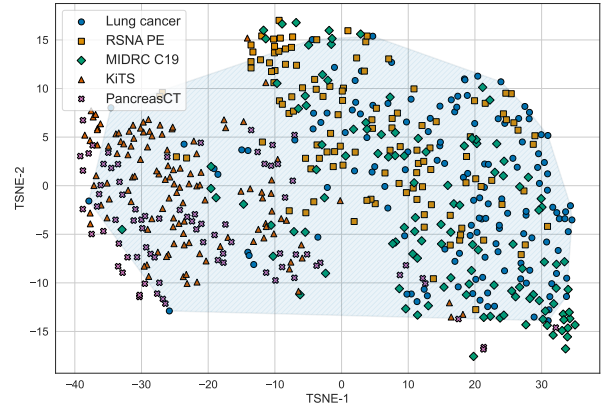
(b) iBOT



(c) SMIT Lite



(d) Swin UNETR



(e) Swin UNETR<sup>†</sup>

Figure C.12: t-SNE projected embeddings showing dataset-wise separability of (a) deep features and (b) radiomics features. Results from one representative split (of 100), combining all datasets in a single visualization, are shown for brevity. The shaded blue regions indicate the convex hull of the ID dataset.